JOURNAL OF AIRCRAFT
Vol. 46, No. 2, March–April 2009

Time-Periodic Stability of a Flapping Insect Wing Structure in Hover

Nicholas C. Rosenfeld* and Norman M. Wereley†
University of Maryland, College Park, Maryland 20742

DOI: 10.2514/1.34938

The wings of insectlike flapping-wing micro air vehicles experience time-periodic inertial stiffnesses during flapping motion. By modeling the wing structure as a thin beam, a linear time-periodic assumed-modes analysis is developed. The equations of motion of a flapping wing undergoing out-of-plane bending and torsion are derived. The homogeneous assumed-modes equations are nondimensionalized. It is shown that the nondimensional strain stiffness varies with the ratio of the wing's nonrotating natural frequencies to the flapping frequency, whereas the nondimensional, time-periodic inertial stiffnesses vary with the amplitudes of flapping and feathering motion. The parametric stability of a representative wing is assessed by applying Floquet analysis to the nondimensional equations of motion, and a scalable stability diagram is presented. Parametric instabilities of the wing structure, caused by time-periodic stiffnesses, are characterized and plotted in the time domain. The effects of important structural design properties on parametric stability are examined.

Nomenclature

$\mathcal{A}$–$\mathcal{Q}$	=	modal coefficient matrices
a	=	constant stiffness
$\boldsymbol{A}(\tau)$	=	state-space matrix
$c(x)$	=	chord
$e(x)$	=	chordwise center of gravity location
$e_A(x)$	=	chordwise centroid location
e_O	=	offset of elastic axis from feathering axis
$EI(x)$	=	bending stiffness
$\boldsymbol{F}$	=	modal forcing vector
$GJ(x)$	=	torsional stiffness
$\boldsymbol{I}$	=	identity matrix
$\boldsymbol{i}, \boldsymbol{j}, \boldsymbol{k}$	=	unit coordinate vectors
$\boldsymbol{K}$	=	nondimensional stiffness matrix
$k_A(x)$	=	polar area radius of gyration
$k_m(x)$	=	polar mass radius of gyration
$m(x)$	=	mass per unit length
N	=	number of assumed modes
$p(x, t)$	=	force loading on wing
$\boldsymbol{Q}$	=	Floquet transition matrix
q	=	pumping stiffness
$q(t)$	=	modal magnitude
$q(x, t)$	=	moment loading on wing
R	=	wing radius
$S_e(x)$, $S_x(x)$	=	mass moments of inertia
t	=	time
$T(x, t)$	=	tension
$w(x, t)$	=	out-of-plane bending displacement
x, y, z	=	rigid-beam coordinates
$\boldsymbol{z}(\tau)$	=	state-space vector
$\gamma(x, t)$	=	torsional displacement
ζ	=	damping
Θ	=	feathering stroke
$\theta(t)$	=	feathering angle
ξ	=	nondimensional spanwise coordinate
τ	=	nondimensional time
Φ	=	flapping stroke
$\phi(t)$	=	flapping angle
$\chi(x)$	=	nonrotating mode shape
ω	=	flapping frequency
ω_w	=	nonrotating bending natural frequency
ω_γ	=	nonrotating torsion natural frequency
$\hat{}$	=	nondimensional distribution
$*$	=	nondimensional time derivative
$\cdot$	=	time derivative

Subscripts

c	=	stiffness coefficient of $\cos\theta$
i, j	=	mode number; matrix index
s	=	stiffness coefficient of $\sin\theta$
w	=	out-of-plane bending value
x, y, z	=	direction in rigid-beam axes
γ	=	torsion value
θ	=	feathering axes; stiffness coefficient of $\hat{\theta}$
ϕ	=	flapping axes; stiffness coefficient of $\hat{\phi}$
ω	=	stiffness coefficient of normalized cantilever frequency
0	=	inertial axes; characteristic value

Superscript

$'$	=	spatial derivative

Introduction

Flapping-wing micro air vehicles (MAVs) have great potential as aerial robotic platforms. Designed to mimic the size and configuration of insects and hummingbirds, it is hoped that flapping-wing MAVs will eventually meet or exceed the flight capabilities of biological fliers, including low-speed maneuverability and hover. Design of such vehicles is hindered by a twofold lack of understanding: an understanding of the mechanisms of biological flight itself and an understanding of how to engineer MAVs to exploit those mechanisms. The biological and, recently, engineering communities have made strides towards the former through detailed and novel studies of biological fliers. Achieving the latter requires generalized analyses based on the underlying physics of flapping flight, analyses which can be difficult to glean from animals evolved to fill specific niches. Our goal in this study is to develop a simple

Presented as Paper 1759 at the AIAA Dynamics Specialists Conference, Honolulu, HI, 23–26 May 2007; received 2 October 2007; revision received 4 July 2008; accepted for publication 10 July 2008.

*Minta Martin Fellow, Department of Aerospace Engineering. Student Member AIAA.

†Professor, Department of Aerospace Engineering. Associate Fellow AIAA.

analytical framework to evaluate the physical stability phenomena and help interpret more complex analyses. We develop a nondimensional, linear time-periodic (LTP) assumed-modes structural analysis of flapping wings for MAVs. We then describe a scalable stability analysis that identifies regions of structural instability arising from the time-periodic inertial loads of flapping flight. This analysis assumes that the effects of aerodynamic forces are small compared with inertial-elastic effects on wing deformations, and so aerodynamics may be modeled as damping or neglected. After providing necessary background information, we derive dimensional assumed-modes equations of motion for a wing undergoing prescribed flapping motion and deforming in out-of-plane bending and torsion. Aerodynamic terms are implicitly included with external forces in the derivation. We nondimensionalize the homogenous bending–torsion equations and identify characteristic parameters describing the periodic stiffness of the system. We show that the strain stiffness is a function of the nonrotating natural frequencies of the wing structure normalized to the frequency of flapping, whereas the periodic inertial stiffnesses are functions of the stroke amplitudes of flapping motion. We develop a stability analysis describing system stability as a function of these physical strain and inertial stiffness parameters. This analysis is used to evaluate the effects of structural design parameters on the stability of the flapping wing. We conclude with a discussion on future work to further extend this analysis.

Background

MAVs are small vehicles, as wide as the palm of your hand (8–15 cm) and weighing no more than a handful of coins (30–90 g) [1]. They are envisioned performing reconnaissance, surveillance, and search-and-locate missions inside buildings, caves, "urban canyons," and other confined environments. Operable MAVs have flown in fixed- and rotary-wing configurations [2–5], but the flapping-wing configuration is particularly attractive because it mimics the proven biological method of small-scale flight. Evolutionary trends have led both insects and hummingbirds (animals whose greatest sizes coincide with MAVs) to use flapping-wing flight. In doing so, they exploit numerous unsteady and low Reynolds number aerodynamic effects to generate lift. Designing an MAV that mimics these effects requires an understanding of the complex interactions between the wing structures and the surrounding aerodynamic environment.

Our study deals with "normal-hovering flight," used by animals possessing only a single pair of functional wings like flies and hummingbirds, or two pairs of wings that act in concert as in bees and butterflies [6]. The natural kinematics of insectlike, normal-hovering flight are well known and are shown in Fig. 1. The primary motion is a flapping rotation in a roughly horizontal stroke plane, sweeping an arc of 110–180 deg. At each end of the arc the wing rotates about its span, flipping so that the upper and lower surfaces reverse orientation. The pitch of the wing is held relatively constant during the up- and downstrokes at 15–30 deg above the stroke plane. Slight out-of-plane motion causes the wing tip to trace an elongated oval or figure-of-eight. Biological fliers produce translational forces by tilting the stroke plane like a helicopter [7]. MAV-sized animals have flapping frequencies ranging from 10–60 Hz [8,9].

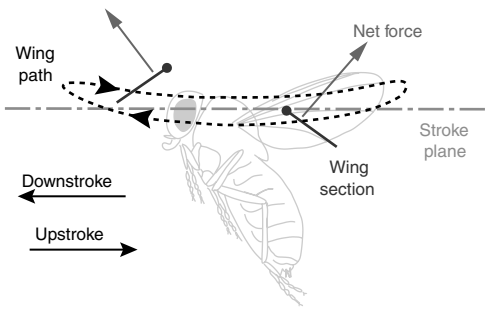

Fig. 1 Wing motion of normal-hovering flight. (Modification of image from [10], used with permission.)

Biological fliers operate in low Reynolds number regimes [8]; animals of similar weight to MAVs have Reynolds numbers on the order of 10^3–10^4. They generate lift by novel aerodynamic mechanisms including attached leading-edge wing vortices, wing–wake effects, the Kramer effect, and clap and fling [11,12]. Recently, simplified analytic aerodynamic models have been developed expressly for MAV applications [13]. The current state-of-the-art analytical aerodynamic models is a time-domain model proposed by Żbikowski [14] and expanded by Ansari, Żbikowski, and Knowles [15,16] that includes several of the preceding aerodynamic effects. This model assumes the wing to be rigid, a poor assumption, as Żbikowski [14] admits. Singh and Chopra [17] have implemented a "loose" aeroelastic coupling of Żbikowski's [14] initally proposed model by iteratively, independently solving for aerodynamic loads and assumed-modes structural deformations of a flapping wing. There is currently no analytic model of insectlike flapping-wing aerodynamics that truly couples with structural deformations, making a fully analytic aeroelastic analysis of insectlike flight a current challenge.

The wings of biological fliers are lightweight, flexible structures that undergo significant bending and torsion deformations during flight. These deformations affect flight forces; for example, torsion–camber coupling provides automatic camber reversal of the wings to increase the lift coefficient [18]. No insectlike biological flier possesses musculature to actively deform its wing. Instead, deformations are the result of inertial and aerodynamic loadings on the wing structure, with inertial forces having significantly greater effect [17,19–21].

In general, biological wings of interest consist of a thick leading-edge spar and thinner trailing spars radiating outward, connected by a flexible surface: respectively, the leading-edge veins, trailing veins, and the wing membrane in insects [8]; and the hand skeleton, feather shafts, and feather vanes in hummingbirds [9]. The literature provides little quantitative data about structural properties of these wings, though some useful studies exist. Combes and Daniel [22] measured average chordwise and spanwise bending stiffnesses of whole insect wings and determined that the leading-edge veins are responsible for the wings' spanwise stiffness. Norberg [23] located the local cross-sectional center of gravity (CG) at different span locations on dragonfly wings and the average elastic axis (EA) location over the entire span. Sunada et al. [24] also measured local CG and EA locations on dragonfly wings and experimentally measured the torsional natural frequencies of dragonfly wings.

Wootton et al.'s survey of modeling techniques for insect wings [25] exhibits the dearth of analytic, physics-based structural models. Of only three "simple analytical models" presented, all are static structural models; no analytic structural dynamics models are included. Not listed in the survey, Sunada et al. [24] analytically modeled the effect of corrugations of dragonfly wings on their torsional stiffness. In contrast, there have been numerous studies modeling insect wings using finite element analysis (FEA) [19,25–29]. FEA has been used to determine wings' structural modes and nonrotational natural frequencies, data that are difficult to measure directly from biological fliers. However, such complex numerical modeling techniques are ill-suited for understanding the role of general structural properties and developing scalable analyses for MAV design.

Several static flapping test stands, as well as a handful of flight-capable MAVs and demonstrators, have been built to collect data from flapping wings and to develop flapping mechanisms for MAVs. Dickinson's Robofly is a Reynolds-scaled aerodynamic test-bed, which operates at low frequencies in a tank of mineral oil [30]. Designed to replicate insect flapping motion and measure the resulting fluid forces, Robofly's high-fidelity data sets have become characteristic data for many biological and engineering analyses. However, Robofly typically uses rigid wings, and so structural and aeroelastic effects are not present. Several open-air test stands have been developed that attempt to match the motion and flapping frequency of biological fliers [31–36]. The goal is elusive: no open-air test stand yet has demonstrated a flapping stroke greater than 90 deg, apparently hindered by difficulties in constructing high-

speed, large-stroke mechanisms (Yan et al. [35] calculate that larger strokes are theoretically possible with advanced four-bar mechanisms). Little useful quantitative structural data have been published from open-air test-stands; only Singh et al.'s study [33] reports basic data such as the wing structure's natural frequencies. The University of Toronto's Mentor is the only insect-inspired vehicle to achieve free hovering flight. It used four flexible wings spaced radially around a vertical fuselage, each flapping 60–75 deg horizontally with the chord fixed perpendicular to the stroke plane. Despite Mentor's success, it too suffers from a lack of published data. A thesis on its wing design qualitatively describes a series of experimental wings and gives representative point measurements of bending and torsion stiffnesses but does not report the wings' natural frequencies or other structural dynamics data [37]. As this article was in press, the 3 cm, 60 mg Harvard Microrobotic Fly became the first true insect-scale flapping MAV to demonstrate tethered flight [38]. Using a bioinspired transmission with a compliant-hinge joint, it reached flapping strokes of 100 + deg. It was equipped with rigid wings during its initial flights.

Because there are gaps in our knowledge of flapping-wing structural dynamics, it is possible to construct poorly designed MAV wing structures. A potential danger of poor design is parametric instability of the wing structure, which may arise in systems having time-periodic parameters [39]. The periodic increase and decrease of a system parameter (stiffness, for example) may cause the system states to diverge regardless of external forcing. A flapping wing is one such system: the motion of the wing creates inertial stiffnesses (e.g., centrifugal stiffness) that are time-periodic functions of rotational velocities and accelerations. If the wing structure is relatively flexible, the inertial stiffnesses may be significant compared with the wing's strain stiffness. It is often unclear whether a particular time-periodic system will suffer parametric instabilities a priori; time-periodic stability analyses are typically needed to assess their stability.

Model Definition

To create a simple analytical model we assume that the bending and torsion loads of the wing are carried through the leading-edge spar. Combes and Daniel [22] show that this is a good assumption for bending deformations, whereas Ennos' study [18] implies it is adequate for torsion deformations. The leading-edge spar is modeled as a thin beam. We assume the wing is symmetric across the cross-sectional thickness and has no initial twist.

The motion of the rigid wing is described by two prescribed angular rotations $\phi(t)$ and $\theta(t)$, defined positive as illustrated in Fig. 2. The flapping angle ϕ describes the wing's position within the stroke plane, whereas the feathering angle[‡] θ describes the inclination of the wing above the stroke plane. Both $\phi(t)$ and $\theta(t)$ are periodic functions of time with a frequency ω. The flapping angle has a stroke of Φ and a median value of $\phi = 0$, whereas the feathering angle has a stroke of Θ and a median value of $\theta = \pi/2$; see Fig. 3.

We define several coordinate axes, also seen in Fig. 2. First are the fixed inertial axes, designated by the coordinates ($\boldsymbol{i}_0$, $\boldsymbol{j}_0$, $\boldsymbol{k}_0$). The flapping axes ($\boldsymbol{i}_\phi$, $\boldsymbol{j}_\phi$, $\boldsymbol{k}_\phi$) rotate about the inertial $\boldsymbol{k}_0$ axis with the flapping angle ϕ. In turn, the feathering axes ($\boldsymbol{i}_\theta, \boldsymbol{j}_\theta, \boldsymbol{k}_\theta$) rotate about the feathering $\boldsymbol{i}_\phi$ axis with the feathering angle θ. The wing's elastic axis lies some offset distance e_O ahead of the axis of feathering rotation. The rigid-beam axes ($\boldsymbol{i}$, $\boldsymbol{j}$, $\boldsymbol{k}$) are defined with the origin at the root of the elastic axis and oriented parallel to the feathering axes. Positions in the rigid-beam coordinates are denoted by the triplet (x, y, z).

Deformations of the wing are measured in the rigid-beam coordinate system, as in Fig. 4. The wing is allowed to undergo bending out of the plane of the wing w and torsion about the elastic axis γ. Positive deformations are as illustrated. Also shown are the locations of the cross section's center of gravity e and area centroid

[‡]In biological studies, this angle is conventionally called the "geometric angle of attack," α. We follow Raney and Slominski's [32] "feathering" terminology to differentiate from the aerodynamic convention defining angles of attack α with respect to the airflow.

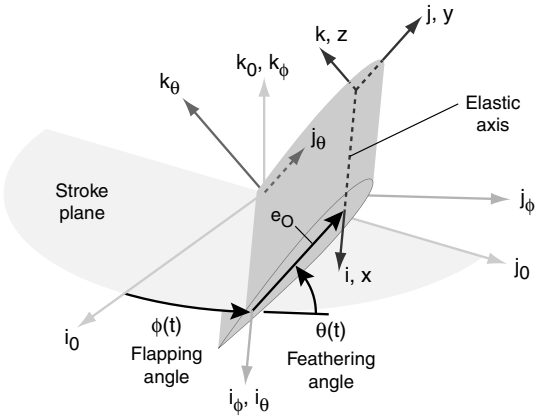

Fig. 2 Coordinate systems for flapping-wing analysis, shown with respect to a rigid wing.

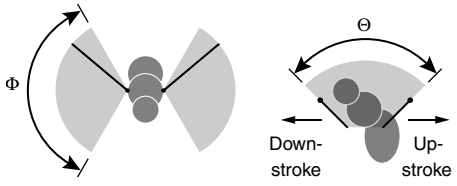

Fig. 3 Flapping stroke Φ and feathering stroke Θ, shown in top and side views of an insect.

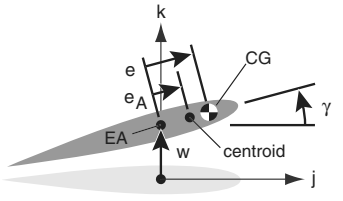

Fig. 4 Cross section of undeflected and deflected wing, shown in rigid-beam coordinate frame.

e_A, both measured positive forward of the elastic axis. Wing bending in the plane of the wing (i.e., in the $\boldsymbol{j}$ direction) is neglected. This is justified by noting that an insect wing cross section has a very large chord compared with its thickness, making it relatively stiff in in-plane bending. Willmott and Ellington [40] measured hawkmoth wing pairs with aspect ratios of 5.28–5.52 and wing thicknesses of .07–.08%R, from which we can estimate average thickness-to-chord ratios on the order of 1.6%, compared with 12–15% for helicopter blades [41].

Estimation of Physical Properties

Before deriving the equations of motion, we need estimates for the structural properties of the wing: the center of gravity offset, the centroid offset, the elastic axis offset, as well as the polar mass radius of gyration k_m, and the polar area radius of gyration k_A; the latter two measured from the elastic axis. Scant quantitative information from biological studies exist on which to base these values. Norberg [23] indicates some values for e and e_A of dragonflies, but no published information gives insight for reasonable values of the radii of gyration. Dudley [8] suggests that the center of gravity is near the axis of feathering rotation to decrease inertial torques.

We create a representative model of a wing cross section to calculate general dimensions for use in this study. The initial geometry is chosen to approximate Norberg's illustrated locations of the EA and CG locations of dragonfly wings. Denoting the wing chord as c, the average location of the elastic axis of the forewing of a dragonfly is $0.21c$ behind the leading edge of the wing, and the location of the center of gravity is $0.31c$ behind the leading edge. The representative wing is modeled as two rectangular sections as shown

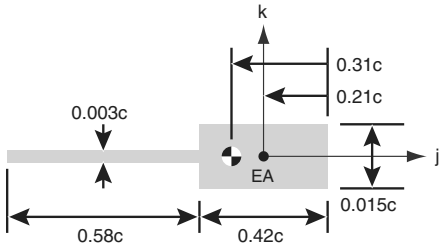

Fig. 5 Representive wing cross section. Not to scale.

in Fig. 5. We assume the small trailing section does not significantly shift the elastic axis away from the centroid of the larger section. The relative thicknesses of the sections locate the CG at $0.31c$ behind the leading edge for a wing of uniform density.

We select the exact thicknesses of the sections to match Combes' measurements of single hawkmoth wings [42]. The mean physical parameters of hawkmoth wings were a wing area of 774 mm^2, a radius of 52.2 mm, and a mass of 44.3 mg. The mean chord is calculated as 14.8 mm and the mean mass-per-unit length is 0.852 mg/mm. Combes reports the average density of hawkmoth wings as 0.5 mg/mm^3. The representative model is scaled to have the same mean mass-per-unit length as the hawkmoth wings for a section of mean chord. The maximum wing thickness is approximately 1.5% of the chord, matching well with the estimated value for insect wings. The representative physical properties are then calculated as functions of c:

$$e = -0.10c \tag{1}$$

$$e_A = -0.10c \tag{2}$$

$$e_O = -e = 0.10c \tag{3}$$

$$k_m^2 = 0.068c^2 \tag{4}$$

$$k_A^2 = 0.068c^2 \tag{5}$$

e and e_A are negative to indicate that they lie behind the elastic axis. The elastic axis offset e_O is set as $-e$ so that the CG is coincident with the feathering axis $\boldsymbol{i}_\theta$, per Dudley [8].

Aerodynamics

Aerodynamic forces on the wing are not explicitly included in the structural model. Biological researchers including Ellington [20] and Ennos [21] have contended that inertial and elastic forces play the primary role in causing wing deformations, with aerodynamic forces being secondary. Recent experimental tests on insect wings and complementary FEA by Combes and Daniel [19] and numerical aeroelastic models by Singh and Chopra [17] indicate an even stronger conclusion: aerodynamic forces play a very small role in determining wing deformations. Combes and Daniel [19] concluded aerodynamic forces primarily provide damping to the wing structure, and the structural dynamics can be adequately calculated from a damped structural model without inclusion of aerodynamic terms. Combes and Daniel approximated the aerodynamic damping as viscous damping proportional to the model's mass matrix. We follow this approach by using a structural, rather than aeroelastic, model of the wing. For simplicity, our derived model and most of the results presented are for an undamped system. Analyses on an equivalent lossy model with linear modal damping indicate that the general conclusions gleaned from the undamped model are valid for the damped model. However, note that aerodynamic forces are implicitly included in the model derivation by the external force distributions, and may be expanded given a suitable analytic aerodynamic model accounting for the influence of wing deformations.

Equilibrium Equations

The derivation of the equations of motion is based on the linear methodology presented in Houbolt and Brooks' [43] study of helicopter blades. This methodology facilitates linear decomposition of the wing dynamics via an assumed-modes method to simplify analysis, as well as application of linear stability analyses. When applied to helicopter blades, Houbolt and Brooks' analysis does not include nonlinear flap–torsion nor flap–lag Coriolis couplings [44] when compared with the nonlinear analysis of Hodges and Dowell [45]. ("Flap" bending by helicopter convention is structurally equivalent to our out-of-plane bending with respect to the airfoil, whereas "lag" bending is equivalent to the neglected in-plane bending.) The latter coupling is moot for the current model, but it stands that there is a nonlinear coupling that this analysis lacks. Furthermore, this analysis has assumed that the structural deflections are small enough to be modeled linearly; if larger deflections occur, a nonlinear model is necessary. Being aware of these deficiencies, we proceed with the analysis.

We consider an untwisted beam element of width dx at a radial position $x\boldsymbol{i}$. The equilibrium equations of this beam element in torsion and out-of-plane bending, respectively, are

$$-[(GJ + Tk_A^2)\gamma']' - Te_A w'' - q_z w' - q_x = 0 \tag{6}$$

$$(EI_z w'' - Te_A\gamma)'' - (Tw')' + q_y' - p_z = 0 \tag{7}$$

Centrifugal tension T is defined by

$$T' = -p_x \tag{8}$$

Force loadings p_x and p_z act in the $+\boldsymbol{i}$ and $+\boldsymbol{k}$ directions, respectively. Moment loadings q_x, q_y, and q_z act at the elastic axis in the $+\boldsymbol{i}$, $-\boldsymbol{j}$, and $+\boldsymbol{k}$ directions, respectively. The beam loadings include inertial forces arising from the prescribed rotations ϕ and θ and external forces acting on the beam. The simplified loadings used in this model are derived in the manner of Houbolt and Brooks [43], and are

$$p_x = m\dot{\phi}^2 x + m(e_O + e)\ddot{\phi}\cos\theta - 2m(e_O + e)\dot{\phi}\,\dot{\theta}\sin\theta \tag{9}$$

$$\begin{aligned} p_z = {} & L_z - m(\ddot{w} + e\ddot{\gamma}) + m\ddot{\phi}x\sin\theta - m\ddot{\theta}(e_O + e) \\ & - m\dot{\phi}^2\sin\theta[(e_O + e)\cos\theta - (w + e\gamma)\sin\theta] + m\dot{\theta}^2(w + e\gamma) \end{aligned} \tag{10}$$

$$\begin{aligned} q_x = {} & M - me\ddot{w} - mk_m^2\ddot{\gamma} + me\ddot{\phi}x(\sin\theta + \gamma\cos\theta) - me\ddot{\theta}e_O - mk_m^2\ddot{\theta} \\ & + me\dot{\phi}^2[w\sin^2\theta - e_O\gamma\cos^2\theta - e_O\sin\theta\cos\theta] \\ & + mk_m^2\dot{\phi}^2[\gamma(\sin^2\theta - \cos^2\theta) - \sin\theta\cos\theta] + me\dot{\theta}^2(w - e_O\gamma) \end{aligned} \tag{11}$$

$$\begin{aligned} q_y = {} & -me\dot{\phi}^2 x\gamma - m(e_O e + k_m^2)\ddot{\phi}\gamma\cos\theta \\ & + 2m(e_O e + k_m^2)\dot{\phi}\,\dot{\theta}\,\gamma\sin\theta \end{aligned} \tag{12}$$

$$q_z = -me\dot{\phi}^2 x - m(e_O e + k_m^2)\ddot{\phi}\cos\theta + 2m(e_O e + k_m^2)\dot{\phi}\,\dot{\theta}\sin\theta \tag{13}$$

L_z and M are external force and moment loadings acting at the elastic axis, including aerodynamic forces. A full derivation of the loadings is presented in [46].

Assumed-Modes Analysis

We return to the beam equilibrium equations, Eqs. (6) and (7). Centrifugal tension T is a function of the prescribed flapping and feathering rotations. This dependence is made explicit by defining mass moments S_x and S_e

$$S_x = \int_x^R mx\,\mathrm{d}x \tag{14}$$

$$S_e = \int_x^R m(e_O + e)\mathrm{d}x \tag{15}$$

and writing T as a function of these mass moments and the prescribed rotations

$$T = -\int_R^x p_x \mathrm{d}x = \int_x^R p_x \mathrm{d}x = \dot{\phi}^2 S_x + (\ddot{\phi}\cos\theta - 2\dot{\phi}\,\dot{\theta}\sin\theta)S_e \tag{16}$$

The equations of motion are solved by applying the modified Galerkin assumed-modes analysis described by Houbolt and Brooks [43], which produces equations equivalent to the Rayleigh–Ritz method. The displacements are approximated by the summation of the first N nonrotational modes

$$\gamma(x,t) = \sum_{i=1}^{N_\gamma} \chi_{\gamma i}(x) q_{\gamma i}(t) = \boldsymbol{\chi}_\gamma^T(x)\boldsymbol{q}_\gamma(t) \tag{17}$$

$$w(x,t) = \sum_{j=1}^{N_w} \chi_{wj}(x) q_{wj}(t) = \boldsymbol{\chi}_w^T(x)\boldsymbol{q}_w(t) \tag{18}$$

where $\chi(x)$ are assumed-mode shapes and $q(t)$ are nondimensional modal magnitudes. A matrix equation is formed for the modal magnitude vectors $\boldsymbol{q}_w$ and $\boldsymbol{q}_\gamma$ by substituting Eqs. (9–13), (17), and (18) into Eqs. (6) and (7) and applying the modified Galerkin method. The resulting matrix equation is

$$\begin{aligned}
&\begin{bmatrix} \mathcal{A} & \mathcal{B} \\ \mathcal{B}^T & \mathcal{C} \end{bmatrix}\begin{Bmatrix} \ddot{\boldsymbol{q}}_\gamma \\ \ddot{\boldsymbol{q}}_w \end{Bmatrix} + \left(\begin{bmatrix} \mathcal{D} & 0 \\ 0 & \mathcal{E} \end{bmatrix} - \ddot{\phi}\cos\theta\begin{bmatrix} \mathcal{F}-\mathcal{G} & -\mathcal{H}+\mathcal{J} \\ (-\mathcal{H}+\mathcal{J})^T & -\mathcal{K} \end{bmatrix}\right. \\
&\quad + \dot{\phi}^2\begin{bmatrix} \mathcal{L} & \mathcal{M}-\mathcal{N} \\ (\mathcal{M}-\mathcal{N})^T & \mathcal{P} \end{bmatrix} - \dot{\phi}^2\sin^2\theta\begin{bmatrix} \mathcal{A} & \mathcal{B} \\ \mathcal{B}^T & \mathcal{C} \end{bmatrix} \\
&\quad + \dot{\phi}^2\cos^2\theta\begin{bmatrix} \mathcal{A}+\mathcal{Q} & 0 \\ 0 & 0 \end{bmatrix} - \dot{\theta}^2\begin{bmatrix} -\mathcal{Q} & \mathcal{B} \\ \mathcal{B}^T & \mathcal{C} \end{bmatrix} \\
&\quad \left. + 2\dot{\phi}\,\dot{\theta}\sin\theta\begin{bmatrix} -\mathcal{G} & -\mathcal{H}+\mathcal{J} \\ (-\mathcal{H}+\mathcal{J})^T & -\mathcal{K} \end{bmatrix}\right)\begin{Bmatrix} \boldsymbol{q}_\gamma \\ \boldsymbol{q}_w \end{Bmatrix} = \begin{Bmatrix} \boldsymbol{F}_{\gamma\mathcal{A}} \\ \boldsymbol{F}_{w\mathcal{A}} \end{Bmatrix} \\
&\quad + \ddot{\phi}\sin\theta\begin{Bmatrix} \boldsymbol{F}_{\gamma\mathcal{B}} \\ \boldsymbol{F}_{w\mathcal{B}} \end{Bmatrix} - \ddot{\theta}\begin{Bmatrix} \boldsymbol{F}_{\gamma\mathcal{C}} \\ \boldsymbol{F}_{w\mathcal{C}} \end{Bmatrix} - \dot{\phi}^2\sin\theta\cos\theta\begin{Bmatrix} \boldsymbol{F}_{\gamma\mathcal{C}} \\ \boldsymbol{F}_{w\mathcal{C}} \end{Bmatrix}
\end{aligned} \tag{19}$$

The integral matrix entries are

$$\begin{aligned}
&\mathcal{A}_{ij} = \mathcal{A}_{ji} = \int_0^R m k_m^2 \chi_{\gamma i}\chi_{\gamma j}\mathrm{d}x \qquad \mathcal{J}_{ij} = \int_0^R e_A S_e \chi_{\gamma i}\chi''_{wj}\mathrm{d}x \\
&\mathcal{B}_{ij} = \int_0^R me\chi_{\gamma i}\chi_{wj}\mathrm{d}x \qquad \mathcal{K}_{ij} = \mathcal{K}_{ji} = \int_0^R S_e\chi'_{wi}\chi'_{wj}\mathrm{d}x \\
&\mathcal{C}_{ij} = \mathcal{C}_{ji} = \int_0^R m\chi_{wi}\chi_{wj}\mathrm{d}x \qquad \mathcal{L}_{ij} = \mathcal{L}_{ji} = \int_0^R k_A^2 S_x\chi'_{\gamma i}\chi'_{\gamma j}\mathrm{d}x \\
&\mathcal{D}_{ij} = \mathcal{D}_{ji} = \int_0^R GJ\chi'_{\gamma i}\chi'_{\gamma j}\mathrm{d}x \qquad \mathcal{M}_{ij} = \int_0^R mex\chi_{\gamma i}\chi'_{wj}\mathrm{d}x \\
&\mathcal{E}_{ij} = \mathcal{E}_{ji} = \int_0^R EI_z\chi''_{wi}\chi''_{wj}\mathrm{d}x \qquad \mathcal{N}_{ij} = \int_0^R e_A S_x\chi_{\gamma i}\chi''_{wj}\mathrm{d}x \\
&\mathcal{F}_{ij} = \mathcal{F}_{ji} = \int_0^R mex\chi_{\gamma i}\chi_{\gamma j}\mathrm{d}x \qquad \mathcal{P}_{ij} = \mathcal{P}_{ji} = \int_0^R S_x\chi'_{wi}\chi'_{wj}\mathrm{d}x \\
&\mathcal{G}_{ij} = \mathcal{G}_{ji} = \int_0^R k_A^2 S_e\chi'_{\gamma i}\chi'_{\gamma j}\mathrm{d}x \qquad \mathcal{Q}_{ij} = \mathcal{Q}_{ji} = \int_0^R me_O e\chi_{\gamma i}\chi_{\gamma j}\mathrm{d}x \\
&\mathcal{H}_{ij} = \int_0^R m(e_O e + k_m^2)\chi_{\gamma i}\chi'_{wj}\mathrm{d}x
\end{aligned} \tag{20}$$

and the forcing vector entries are

$$\begin{aligned}
&F_{\gamma\mathcal{A}i} = \int_0^R M\chi_{\gamma i}\mathrm{d}x \qquad F_{w\mathcal{A}i} = \int_0^R L_z\chi_{wi}\mathrm{d}x \\
&F_{\gamma\mathcal{B}i} = \int_0^R mex\chi_{\gamma i}\mathrm{d}x \qquad F_{w\mathcal{B}i} = \int_0^R mx\chi_{wi}\mathrm{d}x \\
&F_{\gamma\mathcal{C}i} = \int_0^R m(e_O e + k_m^2)\chi_{\gamma i}\mathrm{d}x \qquad F_{w\mathcal{C}i} = \int_0^R m(e_O + e)\chi_{wi}\mathrm{d}x
\end{aligned} \tag{21}$$

Nondimensional Analysis

The linear, time-periodic matrix equations of the flapping-wing deformations given in Eq. (19) are the basis of our time-periodic structural stability analysis. Only the homogeneous system of equations need be considered for the purposes of the stability analysis. A scalable stability analysis is developed by nondimensionalizing the system of equations with respect to characteristic parameters: the system's normalized nonrotating natural frequencies and the stroke amplitudes of the prescribed rigid-beam rotations.

Nondimensional length and time variables ξ and τ are thus introduced:

$$\xi = x/R \tag{22}$$

$$\tau = \omega t \tag{23}$$

Nondimensional structural distributions are defined as follows. Length distributions (including bending-mode shapes) are nondimensionalized with respect to the beam radius R:

$$\hat{\chi}_{wi}(\xi) = \chi_{wi}(\xi R)/R \tag{24}$$

$$\hat{c}(\xi) = c(\xi R)/R, \text{etc.}\ldots. \tag{25}$$

and the torsion-mode shapes retain their value in radians

$$\hat{\chi}_{\gamma i}(\xi) = \chi_{\gamma i}(\xi R) \tag{26}$$

Mass and stiffness distributions are nondimensionalized by some convenient characteristic value:

$$\hat{m}(\xi) = m(\xi R)/m_0, \text{etc.}\ldots. \tag{27}$$

Flapping and feathering rotation distributions are nondimensionalized by their respective amplitudes.

$$\hat{\phi}(\tau) = \begin{cases} \phi(\frac{\tau}{\omega})/(\Phi/2) & \Phi \neq 0 \\ 0 & \Phi = 0 \end{cases} \tag{28}$$

$$\hat{\theta}(\tau) = \begin{cases} \theta(\frac{\tau}{\omega})/(\Theta/2) & \Theta \neq 0 \\ 0 & \Theta = 0 \end{cases} \tag{29}$$

The homogeneous version of the equation of motion Eq. (19) is now rearranged into a nondimensional form:

$$\begin{aligned}
&\begin{bmatrix} \hat{\mathcal{A}} & \hat{\mathcal{B}} \\ \hat{\mathcal{B}}^T & \hat{\mathcal{C}} \end{bmatrix}\begin{Bmatrix} \overset{**}{\boldsymbol{q}}_\gamma \\ \overset{**}{\boldsymbol{q}}_w \end{Bmatrix} + \left(\frac{1}{\bar{\omega}^2}\begin{bmatrix} \frac{GJ_0}{m_0R^4}\hat{\mathcal{D}} & 0 \\ 0 & \frac{EI_{z0}}{m_0R^4}\hat{\mathcal{E}} \end{bmatrix}\right. \\
&\quad - \frac{\Phi}{2}\overset{**}{\hat{\phi}}\cos\theta\begin{bmatrix} \hat{\mathcal{F}}-\hat{\mathcal{G}} & -\hat{\mathcal{H}}+\hat{\mathcal{J}} \\ (-\hat{\mathcal{H}}+\hat{\mathcal{J}})^T & -\hat{\mathcal{K}} \end{bmatrix} \\
&\quad + \frac{\Phi^2}{4}\overset{*2}{\hat{\phi}}\begin{bmatrix} \hat{\mathcal{L}} & \hat{\mathcal{M}}-\hat{\mathcal{N}} \\ (\hat{\mathcal{M}}-\hat{\mathcal{N}})^T & \hat{\mathcal{P}} \end{bmatrix} - \frac{\Phi^2}{4}\overset{*2}{\hat{\phi}}\sin^2\theta\begin{bmatrix} \hat{\mathcal{A}} & \hat{\mathcal{B}} \\ \hat{\mathcal{B}}^T & \hat{\mathcal{C}} \end{bmatrix} \\
&\quad + \frac{\Phi^2}{4}\overset{*2}{\hat{\phi}}\cos^2\theta\begin{bmatrix} \hat{\mathcal{A}}+\hat{\mathcal{Q}} & 0 \\ 0 & 0 \end{bmatrix} - \frac{\Theta^2}{4}\overset{*2}{\hat{\theta}}\begin{bmatrix} -\hat{\mathcal{Q}} & \hat{\mathcal{B}} \\ \hat{\mathcal{B}}^T & \hat{\mathcal{C}} \end{bmatrix} \\
&\quad \left. + \frac{\Phi\Theta}{2}\overset{*}{\hat{\phi}}\overset{*}{\hat{\theta}}\sin\theta\begin{bmatrix} -\hat{\mathcal{G}} & -\hat{\mathcal{H}}+\hat{\mathcal{J}} \\ (-\hat{\mathcal{H}}+\hat{\mathcal{J}})^T & -\hat{\mathcal{K}} \end{bmatrix}\right)\begin{Bmatrix} \boldsymbol{q}_\gamma \\ \boldsymbol{q}_w \end{Bmatrix} = 0
\end{aligned} \tag{30}$$

The hatted matrices are given by Eq. (20), appropriately nondimensionalized.

Equation (30) can be fully nondimensionalized by multiplying it by the inverted mass matrix,

$$\begin{bmatrix} \hat{\mathcal{A}} & \hat{\mathcal{B}} \\ \hat{\mathcal{B}}^T & \hat{\mathcal{C}} \end{bmatrix}^{-1}$$

Additional manipulation is necessary to explicitly parameterize the equation in terms of the normalized nonrotating structural frequencies. The product of the inverse mass matrix and the leading constant stiffness matrix is written as the product of a coupling matrix and a block-diagonal matrix as

$$\begin{bmatrix} \hat{\mathcal{A}} & \hat{\mathcal{B}} \\ \hat{\mathcal{B}}^T & \hat{\mathcal{C}} \end{bmatrix}^{-1} \begin{bmatrix} \frac{GJ_0}{m_0R^4}\hat{\mathcal{D}} & 0 \\ 0 & \frac{EI_{z0}}{m_0R^4}\hat{\mathcal{E}} \end{bmatrix} = \begin{bmatrix} \boldsymbol{I} & \hat{\mathcal{A}}^{-1}\hat{\mathcal{B}} \\ \hat{\mathcal{C}}^{-1}\hat{\mathcal{B}}^T & \boldsymbol{I} \end{bmatrix}^{-1} \begin{bmatrix} \frac{GJ_0}{m_0R^4}\hat{\mathcal{A}}^{-1}\hat{\mathcal{D}} & 0 \\ 0 & \frac{EI_{z0}}{m_0R^4}\hat{\mathcal{C}}^{-1}\hat{\mathcal{E}} \end{bmatrix} \tag{31}$$

The term $\widehat{\mathcal{A}}^{-1}\widehat{\mathcal{D}}$ represents the nonrotational modal torsional stiffnesses normalized by the modal polar mass moments of inertia. Likewise, $\widehat{\mathcal{C}}^{-1}\widehat{\mathcal{E}}$ represents the nonrotational modal bending stiffnesses normalized by the modal masses. These relationships allow the equation to be rewritten in terms of the *uncoupled, nonrotating* torsional and bending natural frequencies. The torsional natural frequencies $\omega_{\gamma i}$ and bending natural frequencies ω_{wj} are functions of the characteristic beam properties [47]

$$\omega_{\gamma i} = (\lambda R)_{\gamma i}\sqrt{\frac{GJ_0}{m_0R^4}}, \qquad i = 1, \ldots, N_\gamma \tag{32}$$

$$\omega_{wj} = (\lambda R)^2_{wj}\sqrt{\frac{EI_{z0}}{m_0R^4}}, \qquad j = 1, \ldots, N_w \tag{33}$$

The nondimensional parameters $(\lambda R)_{\gamma i}$ and $(\lambda R)_{wj}$ depend on the beam's structural distributions and assumed modes. For a general assumed-modes system, the parameters corresponding to the first natural frequencies are

$$(\lambda R)^2_{\gamma 1} = \min \operatorname{eig}(\widehat{\mathcal{A}}^{-1}\widehat{\mathcal{D}}) \tag{34}$$

$$(\lambda R)^4_{w1} = \min \operatorname{eig}(\widehat{\mathcal{C}}^{-1}\widehat{\mathcal{E}}) \tag{35}$$

Multiplying Eq. (30) by the inverse mass matrix and using Eqs. (31–35), the final nondimensional bending–torsion equation is:

$$\begin{Bmatrix} \overset{**}{q}_\gamma \\ \overset{**}{q}_w \end{Bmatrix} + [(\omega_{w1}/\omega)^2\boldsymbol{K}_{\boldsymbol{\omega}} - \Phi\overset{**}{\hat{\phi}}\cos\theta\boldsymbol{K}_{\overset{**}{\boldsymbol{\phi c}}} + \Phi^2\overset{*2}{\hat{\phi}}\,\boldsymbol{K}_{\overset{*2}{\boldsymbol{\phi}}} - \Phi^2\overset{*2}{\hat{\phi}}\sin^2\theta\boldsymbol{K}_{\overset{*2}{\boldsymbol{\phi}}\overset{*2}{\boldsymbol{s}}} + \Phi^2\overset{*2}{\hat{\phi}}\cos^2\theta\boldsymbol{K}_{\overset{*2}{\boldsymbol{\phi}}\overset{*2}{\boldsymbol{c}}} - \Theta^2\overset{*2}{\hat{\theta}}\,\boldsymbol{K}_{\overset{*2}{\boldsymbol{\theta}}} + \Phi\Theta\overset{*}{\hat{\phi}}\overset{*}{\hat{\theta}}\sin\theta\boldsymbol{K}_{\overset{**}{\boldsymbol{\phi\theta s}}}]\begin{Bmatrix} \boldsymbol{q}_\gamma \\ \boldsymbol{q}_w \end{Bmatrix} = 0 \tag{36}$$

The stiffness matrices in Eq. (36) are

$$\boldsymbol{K}_{\boldsymbol{\omega}} = \begin{bmatrix} \boldsymbol{I} & \widehat{\mathcal{A}}^{-1}\widehat{\mathcal{B}} \\ \widehat{\mathcal{C}}^{-1}\widehat{\mathcal{B}}^T & \boldsymbol{I} \end{bmatrix}^{-1} \begin{bmatrix} (\frac{\omega_{\gamma 1}}{\omega_{w1}})^2\frac{1}{(\lambda R)^2_{\gamma 1}}\widehat{\mathcal{A}}^{-1}\widehat{\mathcal{D}} & 0 \\ 0 & \frac{1}{(\lambda R)^4_{w1}}\widehat{\mathcal{C}}^{-1}\widehat{\mathcal{E}} \end{bmatrix}$$

$$\boldsymbol{K}_{\overset{**}{\boldsymbol{\phi c}}} = \frac{1}{2}\begin{bmatrix} \widehat{\mathcal{A}} & \widehat{\mathcal{B}} \\ \widehat{\mathcal{B}}^T & \widehat{\mathcal{C}} \end{bmatrix}^{-1}\begin{bmatrix} \widehat{\mathcal{F}} - \widehat{\mathcal{G}} & -\widehat{\mathcal{H}} + \widehat{\mathcal{J}} \\ (-\widehat{\mathcal{H}} + \widehat{\mathcal{J}})^T & -\widehat{\mathcal{K}} \end{bmatrix}$$

$$\boldsymbol{K}_{\overset{*2}{\boldsymbol{\phi}}} = \frac{1}{4}\begin{bmatrix} \widehat{\mathcal{A}} & \widehat{\mathcal{B}} \\ \widehat{\mathcal{B}}^T & \widehat{\mathcal{C}} \end{bmatrix}^{-1}\begin{bmatrix} \widehat{\mathcal{L}} & \widehat{\mathcal{M}} - \widehat{\mathcal{N}} \\ (\widehat{\mathcal{M}} - \widehat{\mathcal{N}})^T & \widehat{\mathcal{P}} \end{bmatrix}$$

$$\boldsymbol{K}_{\overset{*2}{\boldsymbol{\phi}}\overset{*2}{\boldsymbol{s}}} = \frac{1}{4}\boldsymbol{I}$$

$$\boldsymbol{K}_{\overset{*2}{\boldsymbol{\phi}}\overset{*2}{\boldsymbol{c}}} = \frac{1}{4}\begin{bmatrix} \widehat{\mathcal{A}} & \widehat{\mathcal{B}} \\ \widehat{\mathcal{B}}^T & \widehat{\mathcal{C}} \end{bmatrix}^{-1}\begin{bmatrix} \widehat{\mathcal{A}} + \widehat{\mathcal{Q}} & 0 \\ 0 & 0 \end{bmatrix}$$

$$\boldsymbol{K}_{\overset{*2}{\boldsymbol{\theta}}} = \frac{1}{4}\begin{bmatrix} \widehat{\mathcal{A}} & \widehat{\mathcal{B}} \\ \widehat{\mathcal{B}}^T & \widehat{\mathcal{C}} \end{bmatrix}^{-1}\begin{bmatrix} -\widehat{\mathcal{Q}} & \widehat{\mathcal{B}} \\ \widehat{\mathcal{B}}^T & \widehat{\mathcal{C}} \end{bmatrix}$$

$$\boldsymbol{K}_{\overset{**}{\boldsymbol{\phi\theta s}}} = \frac{1}{2}\begin{bmatrix} \widehat{\mathcal{A}} & \widehat{\mathcal{B}} \\ \widehat{\mathcal{B}}^T & \widehat{\mathcal{C}} \end{bmatrix}^{-1}\begin{bmatrix} -\widehat{\mathcal{G}} & -\widehat{\mathcal{H}} + \widehat{\mathcal{J}} \\ (-\widehat{\mathcal{H}} + \widehat{\mathcal{J}})^T & -\widehat{\mathcal{K}} \end{bmatrix}$$

Comments on Nondimensional Analysis

We now examine the nondimensional system in Eq. (36) more closely. The stiffness matrices $\boldsymbol{K}$ are nondimensional functions of structural distributions (i.e., $\hat{m}$, $\hat{e}$, etc.). The leading stiffness term, written here in expanded form

$$\left(\frac{\omega_{w1}}{\omega}\right)^2\begin{bmatrix} \boldsymbol{I} & \widehat{\mathcal{A}}^{-1}\widehat{\mathcal{B}} \\ \widehat{\mathcal{C}}^{-1}\widehat{\mathcal{B}}^T & \boldsymbol{I} \end{bmatrix}^{-1} \begin{bmatrix} (\frac{\omega_{\gamma 1}}{\omega_{w1}})^2\frac{1}{(\lambda R)^2_{\gamma 1}}\widehat{\mathcal{A}}^{-1}\widehat{\mathcal{D}} & 0 \\ 0 & \frac{1}{(\lambda R)^4_{w1}}\widehat{\mathcal{C}}^{-1}\widehat{\mathcal{E}} \end{bmatrix}$$

represents the strain stiffness of the wing structure subject to forced, but nonrotational, oscillations at a frequency ω. The magnitude of the strain stiffness is characterized by the squared ratio of the wing's lowest nonrotational bending frequency ω_{w1} to the flapping frequency ω; such a relationship is expected from the basic theory of structural dynamics [47]. In this study we will assume cantilever-free beam modes, and for convenience we call the ratio ω_{w1}/ω the "normalized cantilever frequency." The second matrix in this term is block diagonal, containing proportional modal stiffness matrices for the uncoupled, nonrotating bending and torsion assumed modes. The ratio of the first nonrotational torsion frequency over first nonrotational bending frequency $\omega_{\gamma 1}/\omega_{w1}$ in this matrix expresses the relative torsion and bending stiffnesses of the system. If the assumed modes are the exact nonrotational modes of the structure, the second matrix will be strictly diagonal. The first matrix expresses bending/torsion modal coupling through the beam's CG offset.

The remaining stiffness terms are time-periodic inertial stiffnesses arising from the prescribed rotational motion of the flapping wing. The magnitudes of these stiffnesses are functions of the flapping and feathering stroke amplitudes Φ and Θ, whereas the time-variations are due to the rotational distributions $\hat{\phi}$ and $\hat{\theta}$. Trigonometric functions of the dimensional feathering angle $\sin\theta$ and $\cos\theta$ are functions of both Θ and $\hat{\theta}$ and thus affect both the magnitude and time variation of the stiffnesses. This is a notable finding: the relative (i.e., nondimensional) magnitudes of time-periodic inertial stiffnesses are dependent on the total *angle* of rotational motion but are independent of the *frequency* at which the motion occurs.

These characteristic parameters allow us to present scalable analyses for flapping systems. Flapping systems with identical structural and rotational nondimensional distributions will have matched strain stiffness if they have an equal normalized cantilever frequency ω_{w1}/ω and nonrotational torsion-to-bending frequency ratio $\omega_{\gamma 1}/\omega_{w1}$. Likewise, the systems will have matched periodic inertial stiffnesses if they have equal flapping and feathering strokes Φ and Θ.

We can apply this knowledge to evaluate the effectiveness of current mechanisms in mimicking biological fliers. Table 1 compares biological fliers, MAVs, and flapping test stands for a simplified case of no feathering rotation $\Theta = 0$ and no torsional

Table 1 Nondimensional flapping parameters of biological fliers and mechanisms

	Φ, deg	ω_{w1}/ω
Insects [48]	110–180	—
Manduca sexta [25,49]	115–120	1.15–1.55
Hummingbirds [50]	120–190	—
Mentor MAV [37]	60–75	—
Microrobotic Fly [38]	100+	$\gg 1$
Robofly test bed [30,51]	60–180	$\gg 1$
University of Maryland test bed [33]	80	.8–5.2
Cranfield University test bed [36]	90	—
NASA Langley test bed [32]	45	~ 1

deformations $\gamma = 0$. Only the Reynolds-scaled Robofly test bed and the Harvard Microrobotic Fly are capable of matching the flapping stroke Φ, and therefore the inertial stiffnesses, of biological fliers. Unfortunately, there are no experimental data of ω_{w1}/ω for normal-hovering biological fliers available. The sole datum in literature is derived from an FEM (finite element analysis) of a *Manduca sexta* hawkmoth wing, indicating that the wing flaps slightly below the first nonrotating bending frequency. There are similarly little data available from mechanical apparatuses. The only experimental data from which ω_{w1}/ω can be quantitatively computed are from the University of Maryland flapping test bed, which is the most flexible wing tested had values similar to insects, but most experiments were performed at ω_{w1}/ω of 2–5. Composite wings on the NASA test bed were operated near resonance of the rotational natural frequency by tuning the flapping frequency via feedback from a wing-mounted strain sensor. The Robofly test bed is typically outfitted with a functionally rigid wing, and so ω_{w1}/ω is very large; likewise the Microrobotic Fly has so far only flown with functionally rigid wings.

Taken together, it is clear that no MAV or test stand has yet produced data that are structurally similar to biological systems. The majority of current open-air flapping mechanisms can not achieve biological fliers' flapping stroke Φ. Development of mechanisms capable of $120 \leq \Phi \leq 180$ deg will allow matching of inertial stiffnesses. The lack of detailed, extensive measurements of biological wings' natural frequencies is the obvious hurdle in matching ω_{w1}/ω ratios. Once target values are established, materials and manufacturing techniques should be assessed for constructing MAV wings.

Bending Stability Analysis

We begin development of a parametric stability analysis by considering a reduced case of Eq. (36). We fix the feathering angle at $\theta = \pi/2$ and assume the wing is rigid in torsion $\gamma = 0$. The wing is thus oriented with its chord pointing nose up as it flaps in the horizontal plane, and it deforms only by bending within the plane of rotation (i.e., equivalent to elastic blade lag in helicopter analysis). The bending deformation is modeled by a single assumed mode $w(x,t) = \chi_{w1}(x)q_{w1}(t)$. The reduced nondimensional equation of motion is

$$\overset{**}{q}_{w1} + [(\omega_{w1}/\omega)^2 + \Phi^2 \overset{*2}{\hat{\phi}} (K_{\phi}^{*2} - K_{\phi s^2}^{*2})]q_{w1} = 0 \qquad (37)$$

where the scalar $K_{\phi}^{*2} = \widehat{\mathcal{P}}_{11}/(4\widehat{\mathcal{C}}_{11})$ and $K_{\phi s^2}^{*2} = 1/4$. This system is similar to the isolated lag motion of a helicopter rotor, where $\Phi^2 \overset{*2}{\hat{\phi}} K_{\phi}^{*2}$ is the centrifugal stiffness and $\Phi^2 \overset{*2}{\hat{\phi}} K_{\phi s^2}^{*2}$ is the centrifugal relaxation.

We simplify further by prescribing harmonic flapping rotation $\hat{\phi} = \cos\tau$. For this case, Eq. (37) becomes a time-periodic scalar Mathieu equation [39] with the form

$$\overset{**}{q}_{w1} + (a - 2q\cos 2\tau)q_{w1} = 0 \qquad (38)$$

The parameters a, constant stiffness, and q, pumping stiffness, characterize the periodicity of the Mathieu equation and are functions of the physical system parameters ω_{w1}/ω and Φ:

$$a = (\omega_{w1}/\omega)^2 + \Phi^2(K_{\phi}^{*2} - .25)/2 \qquad (39)$$

$$q = \Phi^2(K_{\phi}^{*2} - .25)/4 \qquad (40)$$

The parametric stability of flapping MAV wings can now be analyzed using the Mathieu equation. The scalar Mathieu equation is a classic time-periodic equation; its stability is well known and can be represented on a Strutt diagram, Fig. 6, as a function of the stiffnesses a and q. The stability boundaries of the Mathieu equation are given by a set of Mathieu functions, which are known analytically as functions of the stiffnesses.

The Strutt diagram is ideal for analyzing the Mathieu equation, but we desire a flapping-wing stability diagram in terms of our physical system parameters ω_{w1}/ω and Φ. Using the relationships in Eqs. (39) and (40), we can transform the Strutt diagram into a new stability diagram showing the effects of independent variations of ω_{w1}/ω and Φ. Before we can perform this transformation, note that the term K_{ϕ}^{*2} in Eqs. (39) and (40) is a function of our assumed bending mode. We therefore need to know the boundary conditions of the wing.

There is relatively little information in the literature from which we can choose boundary conditions. Most structural studies in both biological and engineering fields assume that the wing is clamped at its root without explicit justification [22,26,28,29]. Herbert et al. [27] note that insect veins typically will rotate at their root but do not include this degree of freedom in their FEM analysis. The boundary conditions of the wing would appear to depend on the means of actuating the flapping motion of the wing, shown in Fig. 7. Figure 7a depicts a wing that is actuated by a moment applied at the pivot. A clamp transfers the moment, constraining the slope of the wing at the wing root and causing a cantilever boundary. Most operational mechanical flappers appear to use this method. Figure 7b diagrams the indirect flapping actuation used by all normal-hovering insects and by the Microrobotic Fly [38]. Muscles apply a force to a movable dorsal plate, the notum, which rotates the wing about its pivot via lever action. The boundary condition of the wing outboard of the pivot can be modeled as a pinned beam with a torsion spring, as in Fig. 7c, where the spring represents the stiffness of the wing inboard of the pivot transmitting the flapping displacement. As an idealized case, we may assume that the wing inboard of the pivot is very (i.e., near infinitely) stiff. This is equivalent to the clamped-free boundary of Fig. 7a , and so we choose this boundary to represent both MAVs and idealized insects. However, because no data exists from which the inboard wing stiffness can be estimated, there may be a discrepancy between actual, nonidealized insect structural dynamics and current MAV studies. Hummingbirds have muscles attached directly to the wing outboard of the pivot, but this case can also be idealized as a clamped boundary condition. For example, the NASA biomimetic flapper [32] mimics the hummingbird actuation method.

Figure 8 illustrates how the Strutt diagram is transformed into the flapping stability diagram. Using Eqs. (39) and (40), we calculate the ranges of a and q associated with physical parameter ranges of

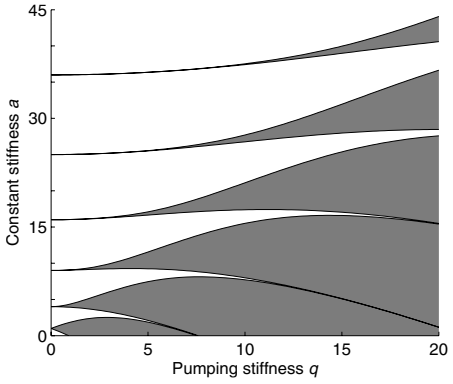

Fig. 6 Strutt diagram of Mathieu equation. Shaded areas are unstable, black lines are exact, analytic stability boundaries.

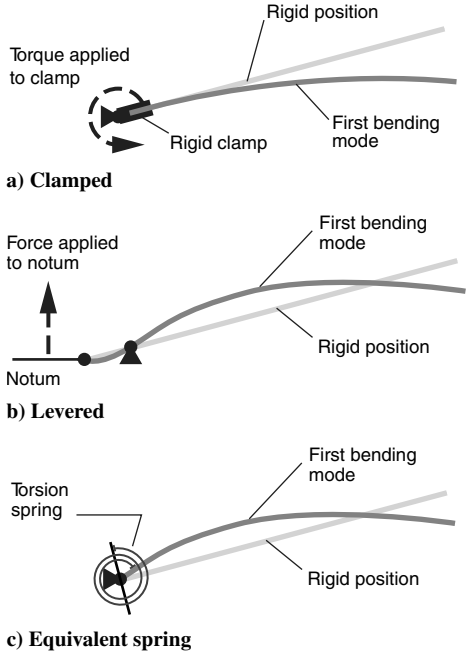

Fig. 7 Effect of flapping actuation on bending-mode boundary condition.

interest $0 \leq \omega_{w1}/\omega \leq 4$ and $0 \leq \Phi \leq \pi$ enclosed by the dashed line in Fig. 8b. By inverting Eqs. (39) and (40), the region of interest on (q, a) is mapped onto $(\Phi, \omega_{w1}/\omega)$, resulting in the stability diagram in Fig. 8c (on the diagram and for the remainder of the paper, Φ and Θ are reported degrees). Only the lowermost Mathieu functions enclose a significant region of instability on this diagram; the Mathieu functions at higher ω_{w1}/ω are essentially zero-thickness lines of marginal stability. This is a typical trend, as parametric instabilities decrease at higher normalized cantilever frequencies. The unstable regions appear relatively benign, occupying only a small portion of the diagram. Furthermore the stability boundaries show little change with Φ, indicating that the modeled structure is relatively aperiodic. We will see that a nonzero feathering stroke Θ and the inclusion of additional modeled modes will increase the instability regions' size and periodicity. Note that these diagrams only represent the periodicity of the unforced wing structure; although the structure may be relatively aperiodic, the forces acting upon it will still be highly periodic.

We use this simple case to illustrate the effect of flapping stroke Φ and normalized cantilever frequency ω_{w1}/ω on the propagation of unforced, undamped instabilities in the time domain. We propagate an initial tip deflection of $\hat{w} = .01$ with an explicit Runge–Kutta solver [52] implemented on FORTRAN 95 for various system parameters. Figure 9 shows the effect of varying Φ (the measure of the system's time-periodic inertial stiffness) as ω_{w1}/ω (and strain stiffness) is held constant. Each alternating white and gray band is, respectively, a downstroke and upstroke of the wing. Because ω_{w1}/ω is fixed, all of these time plots represent wings that are flapped at the same frequency. As Φ increases, so does the natural frequency of the rotating wing, as can be seen by comparing the crests and troughs of tip deformation plots. When the rotating natural frequency approaches a harmonic of the flapping frequency, as in case E, parametric instabilities occur. Case D is close to, but not in, the region of instability; the deformations initially grow but the system is stable overall. It must be stressed that these instabilities are *not* caused by inertial forcing of the beam. Because we are considering a homogeneous system, forcing does not play a role in these instabilities. Rather, they are wholly the result of the periodic inertial stiffnesses arising from the flapping rotation.

Similar results are seen when ω_{w1}/ω is varied at a fixed Φ, as in Fig. 10. Here, strain stiffness changes with ω_{w1}/ω as inertial stiffness is held constant. The wing's rotating natural frequency increases with ω_{w1}/ω. As before, parametric instabilities occur when the wing's rotating natural frequency is near a harmonic of the flapping frequency. However in contrast to Fig. 9, these plots represent wings flapped at different frequencies. If we assume a constant ω_{w1} for a given wing, the dimensional time t corresponding to one period of nondimensional time τ is proportional to ω_{w1}/ω. Finally, note that the single-mode system is more sensitive to changes of its constant strain stiffness than its time-periodic inertial stiffness, hence the more pronounced change in the rotating natural frequency with ω_{w1}/ω than with Φ.

Floquet Analysis

The single-mode stability diagram of Fig. 8c is a transformation of the analytic Mathieu functions. Analytic solutions do not exist for more complex systems. In general, stability diagrams are generated by numerically evaluating the system stability on a discrete mesh of $(\Phi, \omega_{w1}/\omega)$. We use Floquet analysis to determine the stability of the linear, time-periodic system [39]. For a particular point $(\Phi, \omega_{w1}/\omega)$, Eq. (36) is transformed into a state-space form

$$\overset{*}{z}(\tau) = \boldsymbol{A}(\Phi, \omega_{w1}/\omega, \tau)z(\tau) \tag{41}$$

where the time-periodic state-space matrix $\boldsymbol{A}$ is a function of the system parameters. This equation is integrated over one period $0 \leq \tau \leq 2\pi$ to construct a transition matrix $\boldsymbol{Q}$ such that

$$z(\tau + 2\pi) = \boldsymbol{Q}(\Phi, \omega_{w1}/\omega)z(\tau) \tag{42}$$

The system at point $(\Phi, \omega_{w1}/\omega)$ is considered unstable if the eigenvalues of $\boldsymbol{Q}(\Phi, \omega_{w1}/\omega)$ satisfy

$$\max |\text{eig}(\boldsymbol{Q})| > 1 + \epsilon \tag{43}$$

where ϵ is a small safety factor to account for numerical errors in the time integration and is set at $\epsilon = 10^{-5}$.

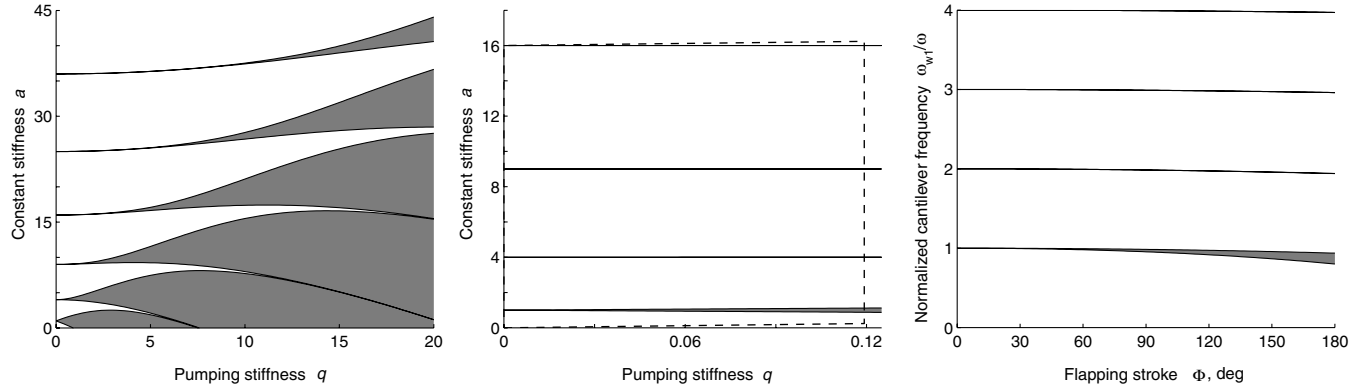

a) Strutt diagram **b) Strutt diagram detail showing stability region** **c) Stability diagram**

Fig. 8 Transformation of Strutt diagram to flapping-wing stability diagram for single bending mode where $\Theta = 0$ deg.

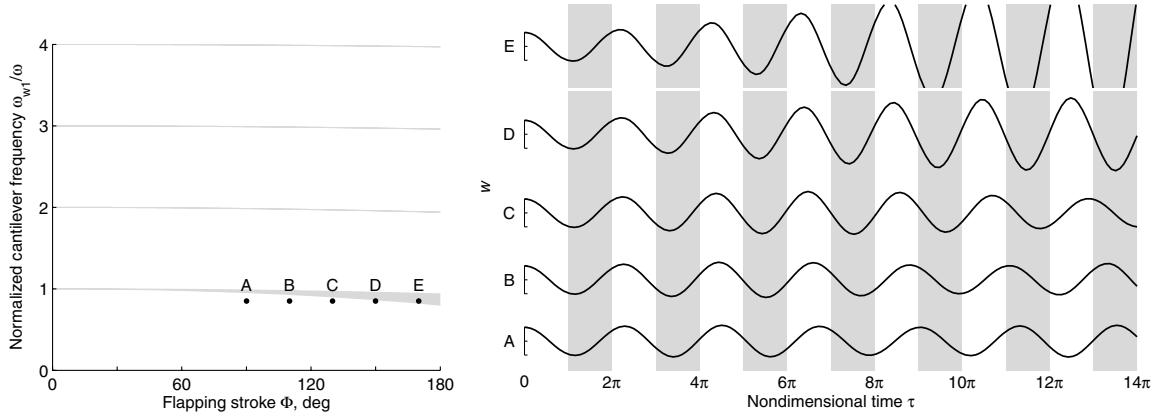

Fig. 9 Propagation of unforced, undamped tip perturbations $\hat{w}$ in single-mode system where $\omega_{w1}/\omega = .85$, $90 \leq \Phi \leq 170$ deg

Bending–Torsion Stability Analysis

With Floquet analysis, we expand our stability analysis to incorporate feathering amplitude Θ and nonzero torsion deformations γ. We first establish baseline physical properties of the flapping-wing model used in the calculation of stability diagrams, and in subsequent analyses, only properties different from the baseline values will be explicitly noted. All diagrams are plotted for the ranges $0 \leq \Phi \leq 180$ deg and $0 \leq \omega_{w1}/\omega \leq 4$. All diagrams are evaluated on square meshes with 601 points per side.

The wing is uniform along its span and has an aspect ratio of 4, similar to hummingbirds (Chai and Millard [50] calculate aspect ratios of 8 for the two-winged full span). The values of $\hat{e}$, $\hat{e}_A$, $\hat{e}_O$, $\hat{k}_m^2$, and $\hat{k}_A^2$ are nondimensionalized from the representative wing presented earlier. Bending deformations are modeled by the first two modes of a cantilever-free uniform beam; torsion deformations by the first mode of a clamped-free uniform beam. Prescribed flapping and feathering rotations are modeled as harmonic motions for simplicity of analysis, a good approximation for insect flapping, though feathering is closer to rounded square wave [7]. In cases where a nonzero feathering stroke is held constant and another parameter is varied, a feathering stroke of $\Theta = 120$ deg is selected as representative of insects [7]. Wootton et al. used an FEM of a hawkmoth wing to calculate its first nonrotational bending frequency as 31 Hz and first nonrotational torsional frequency as 88 Hz [25]; we therefore choose the same ratio of torsion-to-bending frequencies. Table 2 summarizes the baseline values.

Flapping and Feathering Rotation

Before adding higher-frequency torsion and bending modes to the model, we examine the effect of feathering stroke amplitude Θ on the single-mode stability diagram, shown in Fig. 11. In each diagram, Θ is held constant while Φ and ω_{w1}/ω vary. Figure 11a redraws the previously considered $\Theta = 0$ deg case with analytic stability boundaries, although the remaining figures are numerically generated. The instability regions at higher ω_{w1}/ω are so thin as to often fall between the numerical grid. The general shapes of the unstable regions are similar at all magnitudes of Θ, but the size of the unstable regions increases with increasing Θ. For larger feathering strokes, the unstable regions associated with the bending-mode instability extend to higher Φ and ω_{w1}/ω than at lower strokes. The shaded region extending from the origin as Θ increases appears to be an additional bending parametric instability affecting systems with low total stiffnesses (i.e., where both strain and inertial stiffnesses are relatively small) associated with feathering-induced periodic stiffnesses.

Though our model is still relatively crude, Fig. 11 already indicates that structures undergoing insectlike flapping and feathering should not be operated at low ω_{w1}/ω because of parametric instabilities. For example, if our representative system has a feathering stroke of $\Theta = 150$ deg, much of the region $\omega_{w1}/\omega < 1.5$ is unstable. Therefore, flapping frequencies greater than two-thirds of the lowest nonrotational bending frequency should be avoided for this structure.

Additional Modes

We now add higher-frequency structural modes to the system, beginning with the first torsion mode. For the special case with no feathering rotation and the CG and the centroid coinciding with the elastic axis ($\hat{e} = \hat{e}_A = 0$), the bending and torsion modes are uncoupled and the modal equations of motion reduce to two uncoupled scalar Mathieu equations. We may apply the analytic transformation of the Strutt diagram separately for each mode and develop an exact stability diagram by overlaying the instability regions, as in Fig. 12a. In this diagram, gray regions are the previously derived bending instability regions and the black lines are

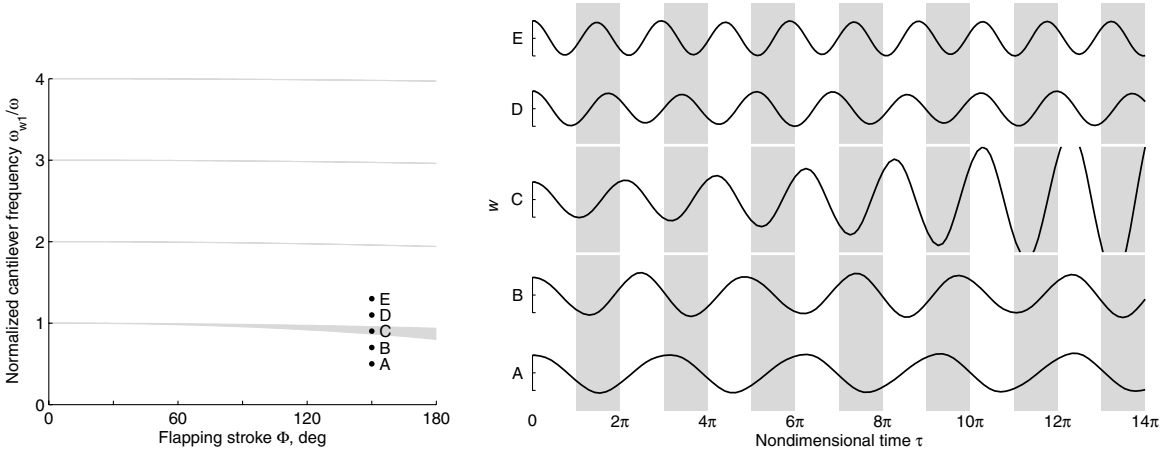

Fig. 10 Propagation of unforced, undamped tip perturbations $\hat{w}$ in single-mode system where $.5 \leq \omega_{w1}/\omega \leq 1.3$, $\Phi = 150$ deg

Table 2 Baseline properties for stability analysis.

Property	Value
N_w, N_γ	2, 1
$\hat{m}, \widehat{EI}_z, \widehat{GJ}$	1
$\hat{c}$	1/4
$\hat{e}, \hat{e}_A, \hat{e}_O, \hat{k}_m^2, \hat{k}_A^2$	see Eqs. (1–5)
$\phi(t)$	$(\Phi/2)\cos(\omega t)$
$\theta(t)$	$(\Theta/2)\sin(\omega t) + \pi/2$
$\omega_{\gamma 1}/\omega_{w1}$	2.84

the boundaries of the torsion-mode instabilities. As with the bending-associated instability regions, the torsion regions at higher ω_{w1}/ω are essentially zero-width lines of marginal stability. Figure 12b shows the stability diagram of the same system generated numerically by Floquet analysis. Again, only the lowest instability regions are thick enough to show up on the mesh. Setting $\hat{e}$ and $\hat{e}_A$ to their nonzero baseline values couples the bending and torsion modes; the resulting matrix equation of motion cannot be solved analytically. Figure 12c shows the numerically generated stability diagram of the coupled case. The additional shaded areas (e.g., the horizontal spike near $\omega_{w1}/\omega = .45$) arise from bending–torsion modal couplings.

The simple, coupled two-mode system allows comparison of the different types of instability regions in the time domain. In Fig. 13, the flapping stroke is held constant at $\Phi = 150$ deg whereas ω_{w1}/ω is varied to create systems with bending, torsion, or coupled bending–torsion instabilities. At each point, two time plots are created: one propagating an initial tip bending deformation of $\hat{w} = .01$ and one propagating an initial tip torsion deformation of $\hat{\gamma} = .01$. Cases E and F show a system unstable in bending. Case E, with an initial tip deformation, clearly shows that the bending natural frequency is near the first harmonic of the flapping frequency, causing the instability. The coupled torsion deformation grows with bending and has an additional frequency component at its own natural frequency, 2.84 times higher than the bending frequency. Case F shows that the initial torsion deformation does not immediately cause the bending deformation to grow quickly, indicating that bending deformations affect torsion more than torsion deformations affect bending. However, the bending deformation is present and will eventually go unstable. Cases A and B show a system unstable in torsion. In these cases, it is the torsion deformation frequency that is near the flapping frequency (recall that lower ω_{w1}/ω corresponds to less dimensional time per period of τ). Both cases clearly go unstable. In case A, the additional frequency component in the bending deformations at 1/2.84 of the torsion frequency is visible. Cases C and D show a system unstable in coupled bending–torsion. As with case F, we see in case D that the initial tip torsion weakly affects the bending deformations. Case C shows the clearer result. Neither bending nor torsion deformations have a frequency near the flapping frequency, which is characteristic of a coupled instability.

Figure 14 shows the stability diagram for the nonfeathering, flapping-wing model as progressively higher coupled modes are included. The leftmost diagram is again the exact single-mode case, the middle diagram adds the first torsion mode ($\omega_{\gamma 1}/\omega_{w1} = 2.84$), and the rightmost adds the second bending mode ($\omega_{w2}/\omega_{w1} = 6.27$). The instability regions associated with higher-frequency modes primarily manifest at lower values of ω_{w1}/ω_w. These are regions where the first-bending-mode instabilities already dominate the diagram for nonzero feathering strokes. Recalling that parametric instabilities decrease at higher normalized cantilever frequencies, we can expect that the instability regions associated with these higher modes will be relatively benign at higher ω_{w1}/ω. Thus, we should expect the parametric instabilities associated with the first bending mode to continue to dominate the system even when higher modes are modeled.

This expectation is borne out when nonzero feathering rotation is applied to the three-mode model. Figure 15 shows the effect of increasing feathering stroke on the three-mode model's stability

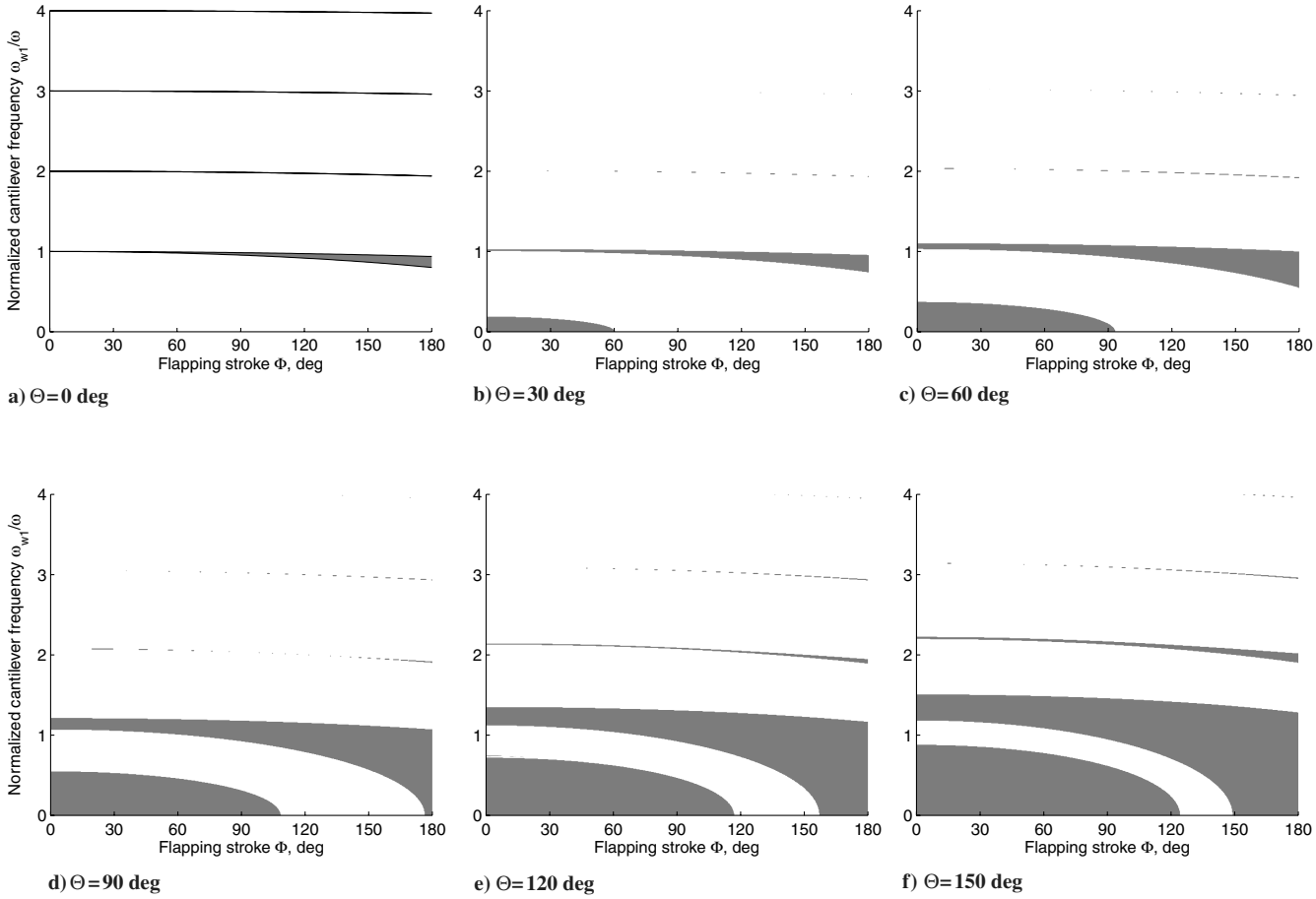

Fig. 11 Effect of feathering stroke Θ on single-mode stability diagram.

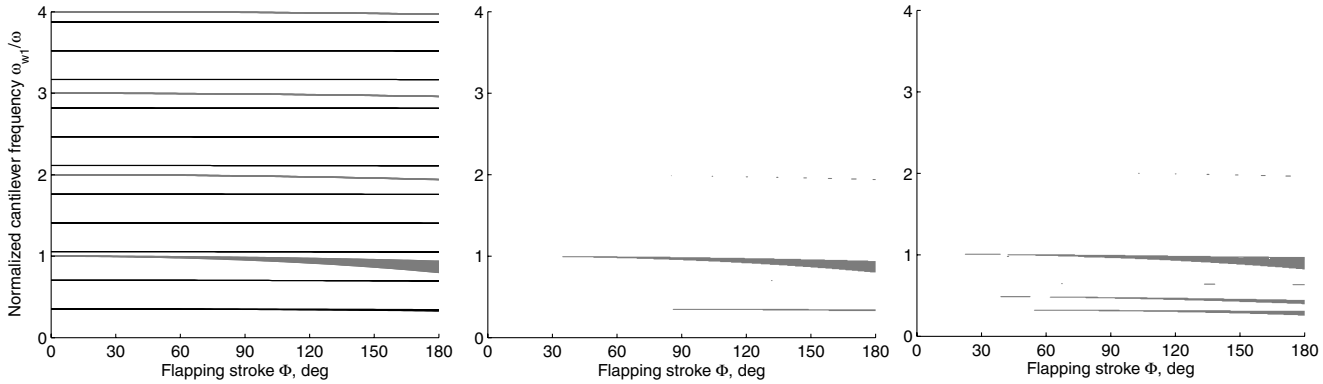

a) Uncoupled, exact **b) Uncoupled, numerical** **c) Coupled**

Fig. 12 Two-mode stability diagram, $\Theta = 0$ deg.

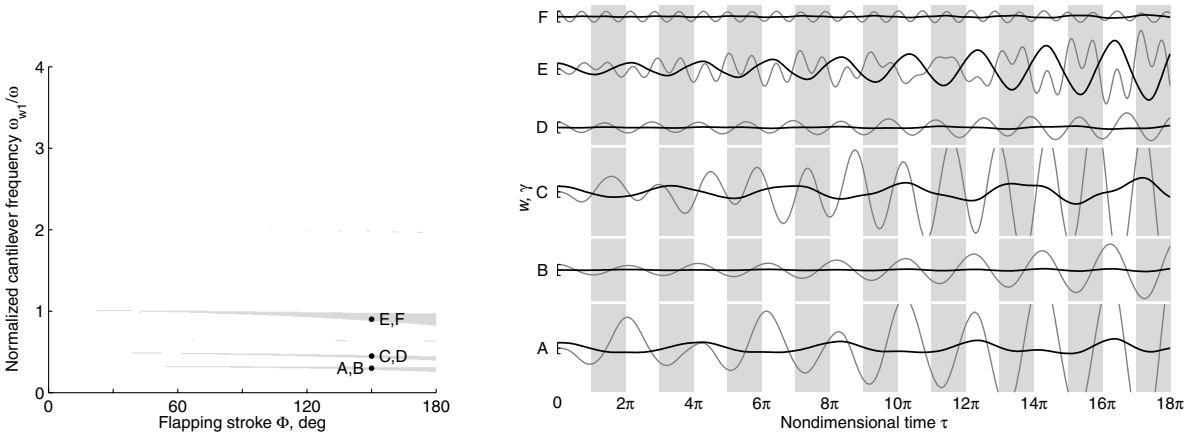

Fig. 13 Propagation of unforced, undamped tip perturbations $\hat{w}$ (black line) and $\hat{\gamma}$ (gray line) in coupled two-mode system where $.3 \leq \omega_{w1}/\omega \leq .9$, $\Phi = 150$ deg.

diagrams. Comparing this to the corresponding single-mode diagrams of Fig. 11 shows that the diagrams are practically identical at higher normalized cantilever frequencies (i.e. $\omega_{w1}/\omega_w > 1.5$). The instabilities associated with higher-frequency structural modes grow (note the nearly horizontal spike at $\omega_{w1}/\omega_w \approx .6$, which is a torsion-associated region) and coalesce. But, these additional regions of instability largely act in regions where the single-mode model already indicated that operation is inadvisable. This suggests that adequate guidelines for avoiding parametric instabilities may be generated with models containing only a few low-frequency modes, but more research is necessary to confirm such a generalization.

Damped Stability

Combes and Daniel [19] concluded that aerodynamic forces on a flapping wing primarily add damping to the system. Damping is included in our nondimensional equations of motion by adding a linear viscous damping matrix $2\zeta \boldsymbol{I}$ multiplying the modal velocity terms. We choose viscous damping as valid for the linear, small-deflection structural model considered in this study. Combes and Daniel do not give data from which a damping parameter ζ can be estimated, and so we must guess at approximately representative values. Figure 16 shows the undamped, flapping and feathering three-mode model along with a slightly damped and significantly damped system. As damping is increased, the thin outlying regions of instability disappear while the larger regions slightly shrink. But even with damping as high as $\zeta = .10$, the general shape and size of the instability regions at low ω_{w1}/ω (the area our stability tests indicate should be avoided) remain unchanged. We can also note that the instability regions associated with higher-frequency modes tend to be eliminated with damping, again lending credence to the concept

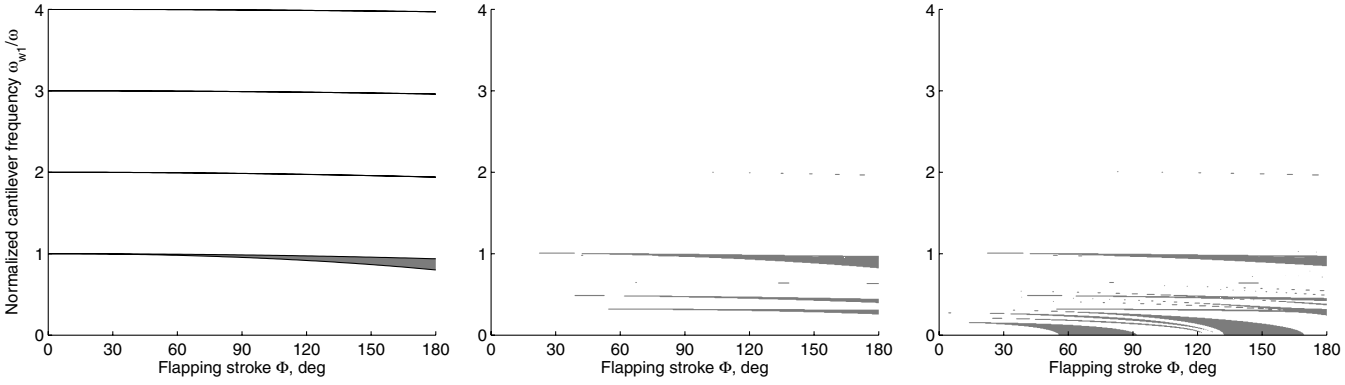

a) One bending mode, exact **b) One bending + one torsion mode** **c) Two bending + one torsion modes**

Fig. 14 Additional coupled modes included on flapping stability diagram where $\Theta = 0$ deg.

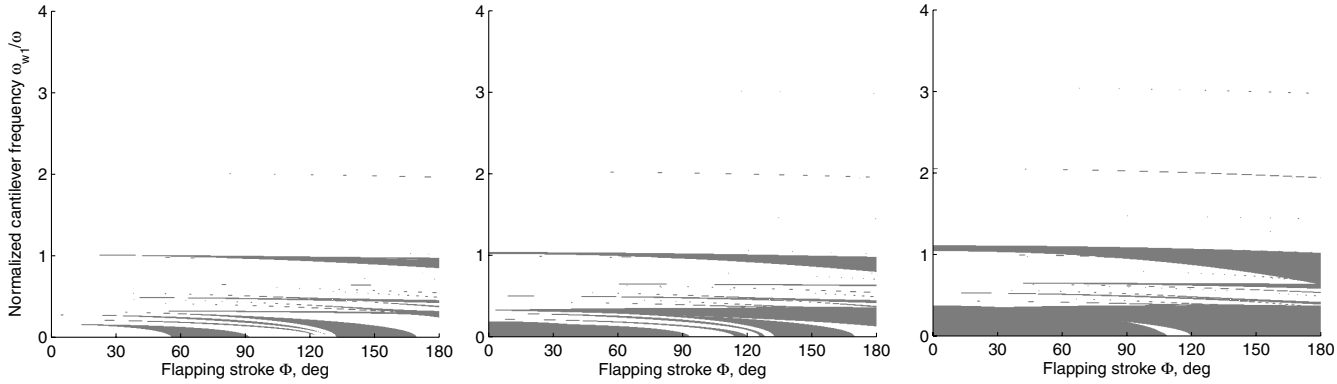

a) Θ = 0 deg **b) Θ = 30 deg** **c) Θ = 60 deg**

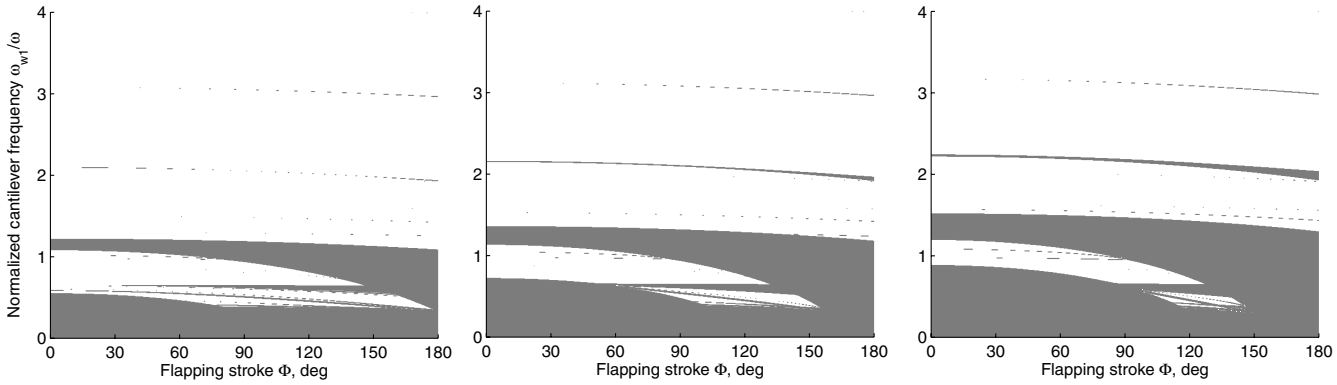

d) Θ = 90 deg **e) Θ = 120 deg** **f) Θ = 150 deg**

Fig. 15 Effect of feathering stroke Θ on three-mode stability diagram.

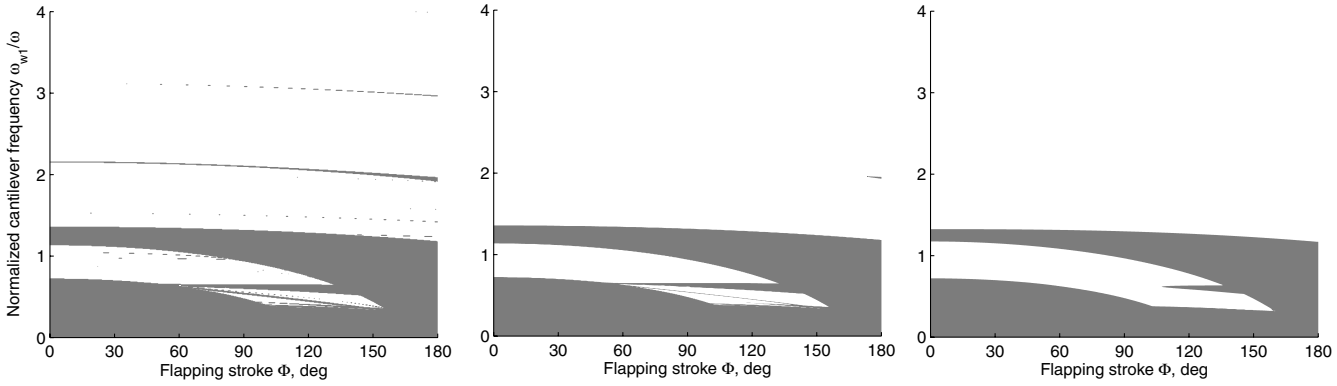

a) ζ = 0 **b) ζ = .02** **c) ζ = .10**

Fig. 16 Effect of constant damping on three-mode stability diagram where Θ = 120 deg.

that perhaps only a small number of modes are necessary to model time-periodic stability of flapping wings.

Location of Center of Gravity

We now return to the undamped model. In rotary-wing systems such as helicopters, the chordwise location of the center of gravity significantly affects system stability [53]. It is therefore instructive to examine the effects of CG on flapping-wing system stability. For the baseline stability diagram, redrawn in Fig. 17a, the baseline CG is 10% chord behind the elastic axis. Figure 17b shows the effect of moving the CG forward to the EA; Fig. 17c moves the CG an additional 10% chord forward. For our model, the CG location does not appear to greatly affect the instability regions associated with the first bending mode, which dominate the diagrams. The CG location does affect the higher-mode instability regions, seen by comparing the areas of $60 \leq \Phi \leq 150$ deg, $\omega_{w1}/\omega < 2/3$. Notably, the horizontal spike (near $\omega_{w1}/\omega = .6$) corresponding to a torsion instability diminishes when the CG coincides with the EA, while the diagonal spike directly below corresponding to a coupled bending–torsion instability strengthens. When the CG is ahead of the EA, both these regions seem equally thick. However, we again see that these changes do not affect the overall character of the stability diagram.

Location of Axis of Feathering Rotation

The elastic axis offset distance $\hat{e}_O$ was chosen so that the CG is coincident with the feathering axis $\boldsymbol{i}_\theta$, in order to reduce inertial torques during feathering rotation. We assess whether this selection has any effect on stability by changing the offset distance. The baseline diagram is given in Fig. 18b, whereas Figs. 18a and 18c move the axis of rotation $\pm 10\%$ chord from the CG along the chord. The effect on stability diagrams is negligible; data comparison shows that Figs. 18a and 18c each differ from the baseline case over only

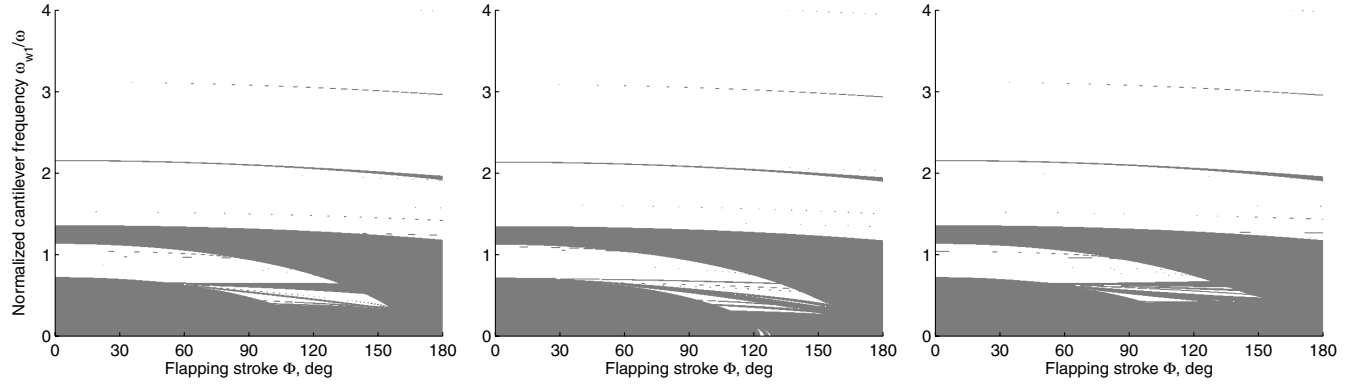

a) CG 0.1*c* behind EA (baseline) **b) CG at EA** **c) CG 0.1*c* ahead of EA**

Fig. 17 Effect of chordwise CG location on three-mode stability diagram where $\Theta = 120$ deg.

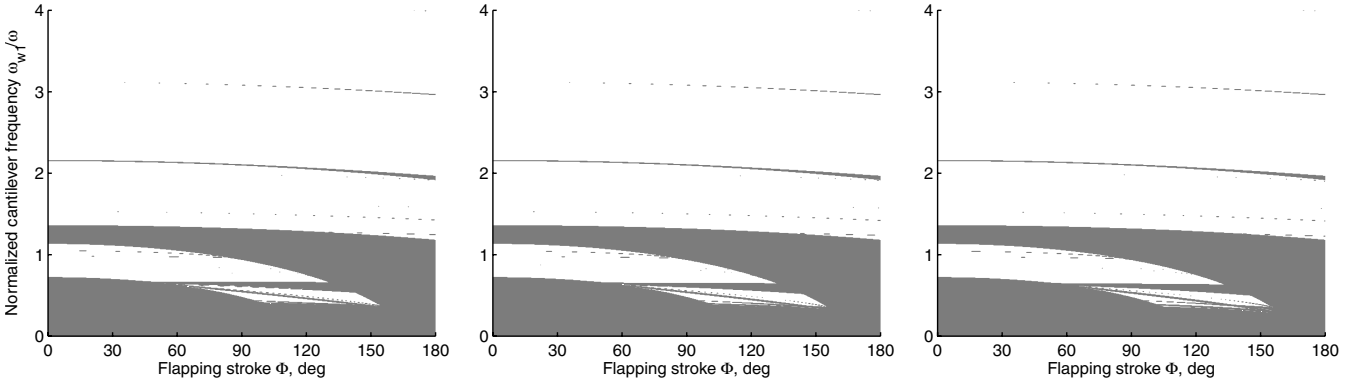

a) Axis of rotation 0.10*c* behind CG **b) Axis of rotation at CG (baseline)** **c) Axis of rotation 0.10*c* ahead of CG**

Fig. 18 Effect of feathering axis location on three-mode stability diagram where $\Theta = 120$ deg.

0.2% of the plotted range, primarily in subtle shifts of higher-mode instability regions. Small changes of $\hat{e}_O$ appear to have almost no effect on system stability.

Conclusion

In this study, we examined the structural parametric stability of an insectlike flapping MAV wing. The wing structure was modeled as a thin beam by assuming the wing's leading-edge spar carried the majority of structural loads. The equations of motion for a thin beam undergoing time-periodic flapping and feathering rotation were derived for a beam experiencing out-of-plane bending and torsion deformations. Aerodynamic loads were not explicitly modeled but were approximated by viscous damping in some cases. We used an assumed-modes analysis to create the dimensional, linear time-periodic matrix equations of motion for the wing system.

We nondimensionalized the homogeneous matrix equation of the flapping wing and characterized the stiffnesses of system with similarity parameters. The normalized cantilever frequency ω_{w1}/ω characterizes the magnitude of the nonrotational strain stiffness of the system. The flapping and feathering strokes Φ and Θ characterize the magnitude of the time-periodic inertial stiffnesses of the system. By comparing the values of these parameters for biological fliers and mechanical apparatuses, we showed that no current mechanical experiment has been structurally similar to biological fliers. Biological fliers appear to operate in regimes that are more susceptible to parametric instabilities, whereas mechanical MAVs and test stands have operated in less-susceptible regimes.

By applying Floquet analysis to the homogenous LTP equations of motion, we generated parametric stability diagrams as functions of the parameters Φ and ω_{w1}/ω. Selected time-domain diagrams illustrated that parametric instabilities occur when a rotating natural frequency of the beam approaches a harmonic of the flapping frequency and confirmed that parametric instabilities can occur without external forcing. A study of the effects of several physical parameters on the time-periodic stability diagrams of a representative flapping wing revealed the following:

1) As a general rule, increasing the normalized cantilever frequency ω_{w1}/ω made a flapping wing less susceptible to parametric instability, whereas increasing the flapping and feathering strokes Φ and Θ made it more susceptible. Detailed modeling is required to determine how changes in parameters will affect a specific system.

2) Regions of instability associated with the lowest bending mode dominated the system stability. Regions of instability associated with torsional modes, higher-frequency bending modes, and coupled modes were less extensive on the diagrams and typically had little effect for normalized cantilever frequencies greater than 1.5.

3) The shape of the regions of instability are relatively independent of the feathering stroke Θ. However, as Θ increases, the extent of the regions of instability increases. Bending instability regions extend to larger values of Φ and ω_{w1}/ω on the diagrams and higher-mode instabilities grow at low values of ω_{w1}/ω.

4) The location of the cross-sectional center of gravity has little effect on the overall stability of the system of our representative wing, primarily affecting the instability regions associated with higher-frequency modes. The location of the feathering axis has almost no effect on system stability.

Though the current results shown here are useful, there is significant room for extension. The linear beam structural model can be refined by considering a nonlinear beam formulation or expanded with a two-dimensional (or higher) structural model. We are currently investigating the latter as ongoing research. In addition to updating the models, a more extensive parametric study of stability with respect to gross system parameters and distributions is necessary to better understand the flapping system. In particular, accurate data of the cross-sectional properties of flapping wings, either from biological fliers or MAVs, can be incorporated into the

model when they become available. This study modeled aerodynamic effects on a small-deformation linear model as viscous damping, but the applicability of other damping models, such as quadratic or fluid damping, should be assessed, particularly for nonlinear extensions of the current analysis. If possible, an accurate unsteady aeroelastic model can be incorporated into the structural model to better understand the interaction between the flapping wing and the surrounding aerodynamic environment. Much is still unknown about the physics and engineering of insectlike MAVs, and we hope that this study will help lay the framework for future advances.

References

[1] Mueller, T. J., and DeLaurier, J. D., "An Overview of Micro Air Vehicle Aerodynamics," *Fixed and Flapping Wing Aerodynamics for Micro Air Vehicle Applications*, edited by T. Mueller, AIAA, New York, 2002, Chap. 1, pp. 1–10.

[2] Bohorquez, F., Samuel, P., Sirohi, J., Pines, D., Rudd, L., and Perel, R., "Design, Analysis and Hover Performance of a Rotary Wing Micro Air Vehicle," *Journal of the American Helicopter Society*, Vol. 48, No. 2, April 2003, pp. 80–90.

[3] Grasmeyer, J. M., and Keennon, M. J., "Development of the Black Widow Micro Air Vehicle," *Fixed and Flapping Wing Aerodynamics for Micro Air Vehicle Applications*, edited by T. Mueller, AIAA, New York, 2002 Chap. 24, pp. 519–535.

[4] Ifju, P. G., "Flexible-Wing-Based Micro Air Vehicles," *Compliant Structures in Nature and Engineering*, edited by C. H. M. Jenkins, WIT Press, Billerica, MA, Chap. 8, 2005, pp. 171–191.

[5] Lipera, L., Colbourne, J. D., Tischler, M. B., Mansur, M. H., Rotkowitz, M. C., and Patangui, P., "The Micro Craft iSTAR Micro Air Vehicle: Control System Design and Testing," *Proceedings of the AHS 57th Annual Forum*, American Helicopter Society, Washington, DC, pp. 1998–2008.

[6] Ellington, C. P., "The Aerodynamics of Hovering Insect Flight: I. The Quasi-Steady Analysis," *Philosophical Transactions of the Royal Society of London B, Biological Sciences*, Vol. 305, No. 1122, Feb. 1984, pp. 1–15. doi:10.1098/rstb.1984.0049

[7] Ellington, C. P., "The Aerodynamics of Hovering Insect Flight: III. Kinematics," *Philosophical Transactions of the Royal Society of London B, Biological Sciences*, Vol. 305, No. 1122, Feb. 1984, pp. 41–78. doi:10.1098/rstb.1984.0051

[8] Dudley, R., *The Biomechanics of Insect Flight: Form, Function, Evolution*, Princeton Univ. Press, Princeton, NJ, 2002.

[9] Videler, J. J., *Avian Flight*, Oxford Univ. Press, New York, NY, 2005.

[10] Dickinson, M. H., Farley, C. T., Full, R. J., Koehl, M. A. R., Kram, R., and Lehman, S., "How Animals Move: An Integrative View," *Science*, Vol. 288, No. 5463, April 2000, pp. 100–106.

[11] Sane, S. P., "The Aerodynamics of Insect Flight," *Journal of Experimental Biology*, Vol. 206, No. 23, Dec. 2003, pp. 4191–4208. doi:10.1242/jeb.00663

[12] Wang, Z. J., "Dissecting Insect Flight," *Annual Review of Fluid Mechanics*, Vol. 37, 2005, pp. 183–210. doi:10.1146/annurev.fluid.36.050802.121940

[13] Ellington, C. P., "The Novel Aerodynamics of Insect Flight: Applications to Micro-Air Vehicles," *Journal of Experimental Biology*, Vol. 202, No. 23, Dec. 1999, pp. 3439–3448.

[14] Żbikowski, R., "On Aerodynamic Modelling of an Insect-Like Flapping Wing in Hover for Micro Air Vehicles," *Philosophical Transactions of the Royal Society of London A*, Vol. 360, No. 1791, Feb. 2002, pp. 273–290.

[15] Ansari, S. A., Żbikowski, R., and Knowles, K., "Non-Linear Unsteady Aerodynamic Model for Insect- Like Flapping Wings in the Hover. Part 1: Methodology and Analysis," *Proceedings of the Institution of Mechanical Engineers, Part G: Journal of Aerospace Engineering*, Vol. 220, No. 2, April 2006, pp. 61–83. doi:10.1243/09544100JAERO49

[16] Ansari, S. A., Żbikowski, R., and Knowles, K., "Non-Linear Unsteady Aerodynamic Model for Insect- Like Flapping Wings in the Hover. Part 2: Implementation and Validation," *Proceedings of the Institution of Mechanical Engineers, Part G: Journal of Aerospace Engineering*, Vol. 220, No. 3, June 2006, pp. 169–186. doi:10.1243/09544100JAERO50

[17] Singh, B., and Chopra, I., "Insect-Based Hover-Capable Flapping Wings for Micro Air Vehicles: Experiments and Analysis," *AIAA Journal*, Vol. 46, No. 9, Sept. 2008, pp. 2115–2135.

[18] Ennos, A. R., "The Importance of Torsion in the Design of Insect Wings," *Journal of Experimental Biology*, Vol. 140, No. 1, Nov. 1988, pp. 137–160.

[19] Combes, S. A., and Daniel, T. L., "Into Thin Air: Contributions of Aerodynamic and Inertial-Elastic Forces to Wing Bending in the Hawkmoth Manduca Sexta," *Journal of Experimental Biology*, Vol. 206, No. 17, Sept. 2003, pp. 2999–3006. doi:10.1242/jeb.00502

[20] Ellington, C. P., "The Aerodynamics of Hovering Insect Flight: VI. Lift and Power Requirements," *Philosophical Transactions of the Royal Society of London B, Biological Sciences*, Vol. 305, No. 1122, Feb. 1984, pp. 145–181. doi:10.1098/rstb.1984.0054

[21] Ennos, A. R., "Inertial and Aerodynamic Torques on the Wings of Diptera in Flight," *Journal of Experimental Biology*, Vol. 142, No. 1, March 1989, pp. 87–95.

[22] Combes, S. A., and Daniel, T. L., "Flexural Stiffness in Insect Wings: I. Scaling and the Influence of Wing Venation," *Journal of Experimental Biology*, Vol. 206, No. 17, Sept. 2003, pp. 2979–2987. doi:10.1242/jeb.00523

[23] Norberg, R. Å., "The Pterostigma of Insect Wings an Inertial Regulator of Pitch," *Journal of Comparative Physiology*, Vol. 81, No. 1, 1972, pp. 9–22. doi:10.1007/BF00693547

[24] Sunada, S., Zeng, L., and Kawachi, K., "The Relationship Between Dragonfly Wing Structure and Torsional Deformation," *Journal of Theoretical Biology*, Vol. 193, No. 1, July 1998, pp. 39–45. doi:10.1006/jtbi.1998.0678

[25] Wootton, R. J., Herbert, R. C., Young, P. G., and Evans, K. E., "Approaches to the Structural Modelling of Insect Wings," *Philosophical Transactions of the Royal Society of London B, Biological Sciences*, Vol. 358, No. 1437, Sept. 2003, pp. 1577–1587. doi:10.1098/rstb.2003.1351

[26] Combes, S. A., and Daniel, T. L., "Flexural Stiffness in Insect Wings: II. Spatial Distribution and Dynamic Wing Bending," *Journal of Experimental Biology*, Vol. 206, No. 17, Sept. 2003, pp. 2989–2997. doi:10.1242/jeb.00524

[27] Herbert, R., Young, P. G., Smith, C. W., Wootton, R. J., and Evans, K. E., "The Hind Wing of the Desert Locust (Schistocerca Gregaria Forskål): III. A Finite Element Analysis of a Deployable Structure," *Journal of Experimental Biology*, Vol. 203, No. 19, Oct. 2000, pp. 2945–2955.

[28] Kesel, A. B., Philippi, U., and Nachtigall, W., "Biomechanical Aspects of the Insect Wing: An Analysis Using the Finite Element Method," *Computers in Biology and Medicine*, Vol. 28, No. 4, July 1998, pp. 423–437. doi:10.1016/S0010-4825(98)00018-3

[29] Smith, M. J. C., "Simulating Moth Wing Aerodynamics: Towards the Development of Flapping-Wing Technology," *AIAA Journal*, Vol. 34, No. 7, July 1996, pp. 1348–1355. doi:10.2514/3.13239

[30] Dickinson, M. H., Lehmann, F.-O., and Sane, S. P., "Wing Rotation and the Aerodynamic Basis of Insect Flight," *Science*, Vol. 284, No. 5422, June 1999, pp. 1954–1960. doi:10.1126/science.284.5422.1954

[31] McIntosh, S. H., Agawal, S. K., and Khan, Z., "Design of a Mechanism for Biaxial Rotation of a Wing for a Hovering Vehicle," *IEEE/ASME Transactions on Mechatronics*, Vol. 11, No. 2, April 2006, pp. 145–153. doi:10.1109/TMECH.2006.871089

[32] Raney, D. L., and Slominski, E. C., "Mechanization and Control Concepts for Biologically Inspired Micro Air Vehicles," *Journal of Aircraft*, Vol. 41, No. 6, Nov.–Dec. 2004, pp. 1257–1265. doi:10.2514/1.5514

[33] Singh, B., Ramasamy, M., Chopra, I., and Leishman, J. G., "Experimental Studies on Insect- Based Flapping Wings for Micro Hovering Air Vehicles," *46th AIAA/ASME/ASCE/AHS/ASC Structures, Structural Dynamics and Materials Conference*, AIAA Paper 2005-2293, April 2005.

[34] Sitti, M., "Piezoelectrically Actuated Four-Bar Mechanism with Two Flexible Links for Micromechanical Flying Insect Thorax," *IEEE/ASME Transactions on Mechatronics*, Vol. 8, No. 1, March 2003, pp. 26–36. doi:10.1109/TMECH.2003.809126

[35] Yan, J., Avadhanula, S. A., Birch, J., Dickinson, M. H., Sitti, M., Su, T., and Fearing, R. S., "Wing Transmission for a Micromechanical Flying Insect," *Journal of Micromechatronics*, Vol. 1, No. 3, 2001, pp. 221–237. doi:10.1163/156856301760132123

[36] Żbikowski, R., Galiński, C., and Pedersen, C. B., "Four-Bar Linkage Mechanism for Insectlike Flapping Wings in Hover: Concept and an Outline of Its Realization," *Journal of Mechanical Design*, Vol. 127, No. 4, July 2005, pp. 817–824. doi:10.1115/1.1829091

[37] Bilyk, D. J., "The Development of Flapping Wings for a Hovering Micro Air Vehicle," Master's Thesis, Univ. of Toronto, Toronto, 2000.

[38] Wood, R. J., "The First Takeoff of a Biologically Inspired At-Scale Robotic Insect," *IEEE Transactions on Robotics and Automation*, Vol. 24, No. 2, April 2008, pp. 341–347.

[39] Richards, J. A., *Analysis of Periodically Time-Varying Systems*, Springer–Verlag, New York, NY, 1983.

[40] Willmott, A. P., and Ellington, C. P., "The Mechanics of Flight in the Hawkmoth Manduca Sexta: II. Aerodynamic Consequences of Kinematic and Morphological Variation," *Journal of Experimental Biology*, Vol. 200, No. 21, Nov 1997, pp. 2723–2745.

[41] Leishman, J. G., *Principles of Helicopter Aerodynamics*, Cambridge Univ. Press, New York, NY, 2nd ed., 2006.

[42] Combes, S. A., *Wing Flexibility and Design for Animal Flight*, Ph.D. Dissertation, Univ. of Washington, July 2002.

[43] Houbolt, J. C., and Brooks, G. W., "Differential Equations of Motion for Combined Flapwise Bending, Chordwise Bending, and Torsion of Twisted Nonuniform Rotor Blades," NACA Report No. 1346, 1958.

[44] Kunz, D. L., "Survey and Comparison of Engineering Beam Theories for Helicopter Rotor Blades," *Journal of Aircraft*, Vol. 31, No. 3, May–June 1994, pp. 473–479. doi:10.2514/3.46518

[45] Hodges, D. H., and Dowell, E. H., "Nonlinear Equations of Motion for the Elastic Bending and Torsion of Twisted Nonuniform Rotor Blades," NASA Technical Note TN-D-7818, 1974.

[46] Rosenfeld, N. C., "Time-Periodic Stability of Flapping Insect and Micro Air Vehicle Wing Structures," Ph.D. Dissertation, Univ. of Maryland, College Park, MD (in preparation).

[47] Meirovitch, L., *Fundamentals of Vibrations*, McGraw–Hill, New York, NY, 2001.

[48] Weis-Fogh, T., "Quick Estimates of Flight Fitness in Hovering Animals, Including Novel Mechanisms for Lift Production," *Journal of Experimental Biology*, Vol. 59, No. 1, Aug. 1973, pp. 169–230.

[49] Willmott, A. P., and Ellington, C. P., "The Mechanics of Flight in the Hawkmoth Manduca Sexta: I. Kinematics of Hovering and Forward Flight," *Journal of Experimental Biology*, Vol. 200, No. 21, Nov. 1997, pp. 2705–2722.

[50] Chai, P., and Millard, D., "Flight and Size Constraints: Hovering Performance of Large Hummingbirds Under Maximal Loading," *Journal of Experimental Biology*, Vol. 200, No. 21, Nov. 1997, pp. 2757–2763.

[51] Sane, S. P., and Dickinson, M. H., "The Control of Flight Force by a Flapping Wing: Lift and Drag Production," *Journal of Experimental Biology*, Vol. 204, No. 15, Aug. 2001, pp. 2607–2626.

[52] Dormand, J. P., and Prince, P. J., "A Family of Embedded Runge–Kutta Formulae," *Journal of Computational and Applied Mathematics*, Vol. 6, No. 1, March 1980, pp. 19–26. doi:10.1016/0771-050X(80)90013-3

[53] Johnson, W., *Helicopter Theory*, Dover, Mineola, NY, 1994.